DOT/FAA/TC-21/31

Federal Aviation Administration
William J. Hughes Technical Center
Aviation Research Division
Atlantic City International Airport
New Jersey 08405

Temperature Responses of Partially Restrained Airfield Rigid Pavement

September 2021

Final Report

U.S. Department of Transportation
Federal Aviation Administration

NOTICE

This report is available at the Federal Aviation Administration William J. Hughes Technical Center’s Full-Text Technical Reports page: actlibrary.tc.faa.gov in Adobe Acrobat portable document format (PDF).

Technical Report Documentation Page

1. Report No.	2. Government Accession No.	3. Recipient's Catalog No.
DOT/FAA/TC-21/31		

4. Title and Subtitle	5. Report Date
TEMPERATURE RESPONSES OF PARTIALLY RESTRAINED AIRFIELD RIGID PAVEMENT	September 2021
	6. Performing Organization Code

7. Author(s)	8. Performing Organization Report No.
Al-Qadi, I.L. and Hernandez, J.	

9. Performing Organization Name and Address	10. Work Unit No. (TRAIS)
Illinois Center for Transportation Department of Civil and Environmental Engineering University of Illinois at Urbana–Champaign 205 North Mathews Avenue, MC-250 Urbana, IL 61801	

12. Sponsoring Agency Name and Address	13. Type of Report and Period Covered
Federal Aviation Administration William J. Hughes Technical Center Headquarters, ACT-9 Atlantic City International Airport, NJ 08405	Final Report

15. Supplementary Notes

The Federal Aviation Administration Aviation Research Division COR for this research project was Dr. Navneet Garg.

16. Abstract

Joint quality affects stresses and deflections, which result from gear and environmental loading, and, hence, short- and long-term performance of rigid pavements. More specifically, multiple researchers have shown that looseness of dowel bars greatly affects responses of Portland cement concrete (PCC) pavement and its performance due to the reduction in load-transfer efficiency. Aware of the relevance of joint efficiency, researchers have used multiple approaches to include it in analyses: closed-form solutions, finite element (FE) analysis, and response from pavement instrumentation. This study combines the three approaches to consider the effect of joint continuity on temperature responses of airfield rigid pavement.

Curling and blowup analysis was performed on airfield rigid pavement, considering generalized boundary conditions. The analysis combined closed-form solutions, FE methods, and pavement instrumentation. Closed-form solutions were derived for the curling responses and stability analysis (i.e., pavement blowup) for a slab-on-grade pavement with partially restrained edges. The closed-form solutions were verified using the FE method. Furthermore, an FE model validated with experimental measurements was used to study the influence of joint condition on the responses to temperature of a multilayer airfield rigid pavement. In general, curling responses and blowup load are significantly affected by the continuity along a slab's edges. Joint condition is more relevant for short slabs, and that aspect ratio is relevant when there is good continuity among slabs. Although conventional analysis does not consider a slab's rotational continuity along the joints, this variable is more relevant than continuity of vertical displacement. Finally, the relevance of rotational continuity increases as the capacity to transfer vertical displacement increases.

17. Key Words	18. Distribution Statement
Partial restraint, Curling responses, Rigid pavement, Pavement blowup	This document is available to the U.S. public through the National Technical Information Service (NTIS), Springfield, Virginia 22161. This document is also available from the Federal Aviation Administration William J. Hughes Technical Center at actlibrary.tc.faa.gov.

19. Security Classif. (of this report)	20. Security Classif. (of this page)	21. No. of Pages	22. Price
Unclassified	Unclassified	66	

ACKNOWLEDGEMENTS

This project was conducted in cooperation with the Illinois Center for Transportation and the Federal Aviation Administration. Dr. Navneet Garg's (FAA) assistance is greatly appreciated. Dr. Osman Erman Gungor's (formerly with the Illinois Center for Transportation) cooperation in calculating the temperature profiles is also acknowledged.

TABLE OF CONTENTS

LIST OF FIGURES

LIST OF TABLES

LIST OF SYMBOLS

A_s:	Dowel's cross-sectional area effective in shear
b:	Twice the ratio between of the slab's width to its length
B_p and B_m:	Addition and subtraction between β_1 and β_2, respectively
c_1, c_2, c_3, c_4:	Constants in general solution of differential equation
D:	Slab's flexural stiffness
E:	Slab's elastic modulus
E_d:	Dowel bar's elastic modulus
h:	Slab's thickness
$i = \sqrt{-1}$:	Complex unity
k:	Dimensionless buckling-load coefficient or modulus of subgrade reaction
k_b:	Product of the dowel-concrete interaction coefficient and the dowel diameter
K_{ij}:	Entries in dowel bar's stiffness matrix (i=1, 2 and j=1, 2)
l:	Radius of relative stiffness
l_{db}:	Length of the bar between slabs (i.e., width of joint)
L:	Slab's length in blowup analysis
LTE:	Load-transfer efficiency
LTE_{dowel}, LTE_{agg}, and LTE_{base}:	LTE provided by dowel bars, aggregates, and base, respectively
LTE-S	Stress-based load-transfer efficiency
M:	Slab's bending moment
N:	Axial load per unit length along slab's edge
N_{critc}:	Critical axial load per unit length along slab's edge
R_a and R_b:	Rotational stiffness indexes along edges a and b, respectively
s and t:	Real and complex part in roots of characteristic equation for Case 3
S_a and S_b:	Translational springs along edges a and b, respectively
S_c:	Dowel bar's stiffness matrix
T_a and T_b:	Translational stiffness indexes
V:	Shear force in the slab
w:	Slab's vertical deflection
$\bar{w}$:	Normalized slab's vertical deflection
x and y:	Normalized coordinates along slab's length and width, respectively
x' and y':	Coordinates along slab's length and width, respectively
$\bar{y}$:	Normalized slab's width
α:	$n\pi$, with n being an integer
β:	Unknown in characteristic equation
β_1 and β_2:	Roots of characteristic equation
δ_{C3}, δ_{C2}, and δ_{C3}:	Critical deflection for conditions C1, C2, and C3, respectively
ΔT:	Temperature gradient
κ_a and κ_b:	Rotational springs
λ:	Dimensionless subgrade-stiffness coefficient

Λ:	Elastic foundation's constant
θ:	Slab's rotation
σ_o:	Maximum curling stress in a fully restrained infinite slab
$\sigma_{c,C1}$, $\sigma_{c,C2}$, and $\sigma_{c,C3}$:	Critical tensile stress for conditions C1, C2, and C3, respectively
$\bar{\sigma}$:	Curling stress normalized with respect to σ_o
ν:	Slab's Poisson's ratio
$[A]$:	Matrix storing coefficient of c_1, c_2, c_3, and c_4
$[C]$:	Vector storing c_1, c_2, c_3, and c_4
$[COEF]$:	Vector of trigonometric functions
$[REM]$:	Terms not multiplying trigonometric functions
$[RT]$:	Vector containing combinations of R_a, R_b, T_a, and T_b
$[TRIG]$:	Matrix storing trigonometric functions' coefficients

LIST OF ACRONYMS

DGAB	Dense-graded aggregate base
EICM	Enhanced integrated climatic model
FAA	Federal Aviation Administration
FEA	Finite element analysis
FE	Finite element
FHWA	Federal Highway Administration
JFK	John F. Kennedy International Airport
MEPDG	Mechanistic-Empirical Pavement Design Guide
PCC	Portland cement concrete
RMSE	Root mean square error

EXECUTIVE SUMMARY

Joint quality affects stresses and deflections, which result from gear and environmental loading, and, hence, short- and long-term performance of rigid pavements. More specifically, multiple researchers have shown that looseness of dowel bars greatly affects responses of Portland cement concrete (PCC) pavement and its performance due to the reduction in load-transfer efficiency. Aware of the relevance of joint efficiency, researchers have used multiple approaches to include it in analyses: closed-form solutions, finite element (FE) analysis, and response from pavement instrumentation. This study combines the three approaches to consider the effect of joint continuity on temperature responses of airfield rigid pavement.

The effects of partially restrained edges and temperature on the responses of airfield rigid pavement were studied using closed-form solutions, FE modeling, and pavement instrumentation. Partial restraints along the edges represent various levels of load-transfer efficiency and were modeled using linear translational and rotational springs. The stiffness of the springs can vary from zero (i.e., no load is transferred) to infinity (i.e., perfect load transfer efficiency). The effect of partially restrained edges on three phenomena—curling responses of slab-on-grade systems, pavement blowup of slab-on-grade systems, and curling responses of a multilayer rigid pavement—were considered. Closed-form solutions were derived using classical approaches, and Westergaard's seminal work on rigid pavement analysis was extended. The solutions provided stresses and deflections for an infinitely long slab-on-grade system subjected to linear temperature distribution. Furthermore, algebraic expressions to calculate blowup load of a rectangular concrete pavement are presented. Finally, multiple layers were included in an ABAQUS FE model and nonlinear temperature profiles were adopted. The model was validated using pavement instrumentation responses.

The results showed that joint quality of airfield rigid pavement affects the pavement's response to temperature. The maximum deflection and stresses caused by linear and nonlinear temperature profiles were affected by the ability of joints to transfer shear force and bending moment across slabs. When considering the free edge as a reference, partial rotational restraint accounted for most of the difference in pavement responses; rotational restraints are not considered in conventional analysis approaches. The influence of partial restraints was evident in the blowup analysis. It was observed that as springs' translational stiffness increased, rotational springs became more relevant. Finally, it was noticed that short slabs' responses were more sensitive to joint condition.

1. INTRODUCTION

1.1 BACKGROUND

Joint quality affects stresses, deflections, and short- and long-term performance of rigid pavements. More specifically, multiple researchers have shown that looseness of dowel bars greatly affects responses of Portland cement concrete (PCC) pavement (Davids & Mahoney, 1999), and that load-transfer efficiency at cracks and joints greatly affects pavement's performance (Khazanovich & Gotlif, 2003). As a result, state highway agencies have invested resources to determine the joint quality. Approximately 38% of states use a falling-weight deflectometer (FWD) to test at corners and edges of rigid pavements (Alavi et al., 2008).

Aware of the relevance of joint continuity, researchers have used multiple approaches to include it in analyses: closed-form solutions, finite element analysis (FEA), and pavement instrumentation. Each approach has its own benefits and drawbacks. FEA is computationally expensive and requires special training, but it can represent virtually any real-life scenario. Pavement instrumentation is very costly but, when done properly, provides the most accurate information. Closed-form solutions can be applied to a limited number of cases but provide an acceptable quality of results almost instantly.

This study combines the three approaches to consider the effect of joint continuity on temperature responses of airfield rigid pavement. First, Westergaard's (1927) solution for temperature responses of slab-on-grade systems was extended to consider partially restrained joints. Maintaining all other Westergaard assumptions unmodified, closed-form solutions for curling stresses and deflections of an infinitely long slab that is partially restrained as to displacement and rotation were derived. After detailing the procedure to find the solutions, the finite element (FE) method validated the proposed model. Subsequently, the effect of partial restraint along the edges, geometry, and material properties of the systems on slab displacements and stresses were studied. Adjustment factors that relate curling responses of slabs, from square to infinitely long, were calculated.

Second, the combined effect of nonlinear temperature profile and slab connectivity on curling stresses and deflections of a multilayer rigid pavement was addressed. Temperature measurements and a modified version of the enhanced integrated climatic model (EICM) predicted temperature profiles. The temperature input covered 5,263 hours and a wide range of average temperatures, temperature gradients, and degrees of nonlinearity. Linear springs in the shear and bending direction simulated slab connectivity, and comparison between measured and predicted strains at the bottom of the slab validated the FE model. The evaluation focused on the tensile stresses and corner deflections, which are related to fatigue life and faulting, respectively.

Third, the phenomenon of pavement blowup was investigated, focusing on the effect of partially restrained edges. Closed-form solutions for the critical load were derived. The proposed equations to calculate blowup load can be applied to concrete pavement with any in-plane dimensions, including infinitely long or wide. Two opposite edges of the slab were partially restrained as to rotation and displacement by assigning translational and rotational elastic springs. Consequently, any combination of classical boundary conditions can be captured in a single stability equation,

including interaction with a rigid structure. The obtained results were successfully compared with expressions assuming classical boundary conditions and values from a FE model.

1.2 OBJECTIVE AND SCOPE

The main objective of this study was to use pavement instrumentation, the FE method, and closed-form solutions to include partially restrained edges in the temperature responses of rigid pavement, focusing on curling and blowup.

1.3 REPORT OVERVIEW

This report consists of seven sections and two appendices. Section 2 summarizes the literature review on the responses of rigid pavement to temperature, focusing on curling and blowup analysis. Section 3 studies slab-on-grade systems and presents a closed-form solution to the stresses and deflections when the slab edges are partially restrained to rotation and displacement. Section 4 examines the system as it is extended to multiple layers, and a FE model is developed to assess the effect of joint condition on curling responses of airfield rigid pavement. Section 5 focuses on blowup analysis of the slab-on-grade system for a slab with partially restrained edges. Section 6 summarizes the main conclusions of this study, and section 7 provides a list of references. Appendix A lists a linear system of equations and solution for slab on-grade systems, and appendix B provides terms in the characteristic stability equation.

2. LITERATURE REVIEW

2.1 CURLING STRESSES IN RIGID PAVEMENT

Curling stresses develop in rigid pavement due to variation in temperature between the top and bottom of the concrete slab. Although curling stresses may not be as significant as vehicular-loading stresses, curling stresses usually result in increased cracking potential and, hence, reduce pavement serviceability and affect long-term performance. Westergaard (1927) conducted one of the first studies on stresses caused by the temperature differential across concrete-slab thickness and proposed closed-form solutions for infinitely long and semi-infinite slabs. In addition to plate theory assumptions (i.e., cross section before bending remains a plane after bending, slab's thickness is small compared to the other dimensions, and vertical strain is negligible (Timoshenko & Woinowsky-Krieger, 1959), Westergaard (1927) assumed linear elastic homogenous concrete, linear temperature distribution throughout the slab's thickness, no loss of support between the slab and the Winkler foundation, and the slab's edges being free to rotate and translate.

Westergaard's closed-form solution has been improved over the years by eliminating some of its assumptions. In 1993, analytical expressions for displacements and stresses considering separation between the slab and the Winkler foundation were derived. The procedure divided the problem into two domains, one for the part in contact with the Winkler foundation (same as Westergaard's equations) and the other one for the lifted part. The equations can be applied to infinitely long and semi-infinite slabs satisfying Westergaard's other assumptions, including free rotation and displacement along the edges (Tang et al., 1993). Similarly, in 1998, Liang and Niu combined thermal and plate analysis to derive closed-form expressions for the temperature distribution and curling stresses of a three-layer concrete pavement. In addition to no restriction to displacement

and rotation along the slab's edges, the main assumption to calculate curling stresses was the decomposition of total deflection into the components along each direction without any coupling. The frequency of temperature variation was more relevant than the magnitude of the temperature variation itself (Liang & Niu, 1998). Finally, Ioannides and his coauthors (1999) combined the FE method and artificial neural networks to assess the implications of Westergaard's assumptions. The most restrictive and consequential assumption of Westergaard is full contact between the PCC and the underlying layer, but the accuracy of the closed-form solution for a slab under load and curling and the other methods was similar.

More specifically, linear temperature distribution has received special attention; and numerous studies have quantified the effect of nonlinear temperature on curling stresses. Regarding linearity, slab temperatures measured over a 9-month period revealed nonlinear profiles on a rigid pavement 9 inches thick (Richardson & Armaghani, 1987). Regarding the effect on curling stresses, linear temperature profiles provided lower curling stresses during evening and early morning hours; the difference in tensile stresses between the linear and nonlinear assumptions was as high as 300% (Mohamed & Hansen, 1997). Similarly, Ioannides and Khazanovich (1998) highlighted the relevance of self-equilibrating stresses, which result from the nonlinear component of the temperature profile. Hiller and Roesler (2010) compared pavement damage and found inaccurate predictions of fatigue life when omitting temperature nonlinearity.

Even though temperature distribution is the driving factor, curling stresses also depend on properties of the PCC, the slab's geometry, the supporting structure (i.e., subbase and subgrade), and connectivity among slabs (Ceylan et al., 2016). The effect of slab connectivity on curling stresses has received minor attention. Some efforts modeled concrete pavement and dowel bars using finite elements, resulting in high computational cost (William and Shoukry, 2001). The main purpose of the finely meshed dowel bars was to investigate the stress state around the dowel bars under various temperature profiles. The frictional interaction between the dowel bars and concrete allowed for partial contact caused by curling, which resulted in a reduction of slab deflection. Deflections from the FE method were smaller than in Westergaard's equations, when assuming a linear temperature gradient. In addition, the difference between the FE method and Westergaard's stresses was 9.3% at the center and 16% at the joints, with the FE method providing higher stresses. Westergaard's analysis was proved useful for the curling component of total thermal stresses in a PCC slab (William & Shoukry, 2001). Following a similar approach, Shoukry et al. (2007) reported small differences between the FE method and Westergaard's solution when using 24-degrees-of-freedom brick elements.

An alternative approach to represent dowel bars and avoid high computational cost is to use them as linear springs. Nishizawa et al. (1996) used such an approach to show insensitivity of curling stresses to shear springs. The rotational springs caused difference in the curling stresses of up to 8% (higher for higher rotational springs) when the temperature gradient was 61°F. The 8% difference was deemed small, and the proposed equation for curling stresses ignored bending springs (Nishizawa et al., 1996). Similarly, Wang and Chen (2011) modified NIKE3D (three-dimensional FE software developed by the Federal Aviation Administration (FAA) for the analysis of airfield rigid pavement), to improve curling calculations. The study considered the effect of the interaction between multiple slabs as shear stress by using linear spring elements.

The influence of dowel-bar looseness on principal stresses in a concrete slab and the impact of the vertical stress on the base layer has been also examined using a FE method. Looseness, which is directly related to the edge condition, increased the maximum principal tensile stress (Davids, 2000) and decreased the load-transfer efficiency (Kim & Hjelmstad, 2003). Davids (2000) used the embedded FE formulation to model the dowel bar. The formulation allowed debonding from the slab and considered the gap around the dowel bar, and the looseness was modeled using the Winkler foundation concept. Kim and Hjelmstad (2003) used Timoshenko beam elements to simulate the dowels. Between 15% and 30% of the wheel load was transferred from one slab to the other by the dowels, with 95% of that transfer being done with the 9 to 11 dowel bars closest to the load (Kim & Hjelmstad, 2003).

FAA Rigid and Flexible Iterative Elastic Layered Design (FAARFIELD), the airfield pavement-design software developed by the FAA, has been used to determine the effect of stress-based load-transfer efficiency on airfield rigid pavement. It was concluded that (1) stress-based load-transfer efficiency, $LTE(S)$, is relevant for thickness design of rigid pavements; and (2) the temperature gradient in the slab influences $LTE(S)$ (Joshi et al., 2012). As for the dowel bar, a stiffness-matrix approach was proposed by Guo et al. (1995). The methodology does not depend on a fine mesh for studying the dowel-concrete interaction and load-transfer mechanism. The stiffness matrix of the dowel bars, which was incorporated in a FE code, was derived assuming three segments for the dowel bar, two embedded in the concrete and one along the joint spacing. A reasonable agreement was reported between measured and calculated dowel-bar responses.

Curling in concrete pavement has also been studied using instrumentation. For instance, curling and temperature measurements indicated that the effect of high-positive-temperature gradients can be decreased because of built-in curling (Yu et al., 1998); and measurement of temperature and strain distribution along the slab's depth showed that they are nonlinear, mainly at the edges of the slab (Wei et al., 2019). Furthermore, curling calculated based on deflections at the slab corners identified upward slab curling and built-in curling as relevant for top-down cracking (Beckemeyer et al., 2002). Using measured deflections at the center of the slab, it was found that a slightly higher curling is caused by a positive temperature differential than by negative one (Siddique et al., 2005). Not many studies using experimental measurements have focused on the slab's edge condition. One of the exceptions is the work of Asbahan and Vandenbossche (2011), who determined the slab's curvature from strain gauge, temperature, moisture, and surface-profile readings. Two types of slabs, restrained (with tie and dowel bars) and unrestrained (no dowel or tie bars), were instrumented. The restrained slab showed 60% lower curvature than the unrestrained one, which underscores the relevance of the boundary conditions along the edges of the slab.

2.2 RIGID-PAVEMENT BLOWUP

Analytical models aimed at studying concrete-pavement blowup lack a proper representation of the boundary conditions. Regardless of slab geometry, material properties, and loading conditions, existing approaches have focused on slabs with classical boundary conditions (i.e., simply supported, clamped, or free). For certain slab geometries such as circular and rectangular, there are exact stability equations as long as the boundaries are either free or fully restrained (Wang et al., 2004).

The buckling of a long slab resting on an elastic foundation, with consideration of the potential detachment between slab and foundation, has been studied previously (Seide,1958), but the stability equation was limited to simply supported slabs. Similarly, stability of an infinitely long and wide slab has been addressed using the Fourier transform (Kim, 2004). The model considered a moving load of constant amplitude, a stationary harmonic load, and a moving harmonic load. Even though static and dynamic stability was captured, the solution cannot be applied to slabs with finite dimensions, such as concrete pavements. Yu and Wang (2008) also studied rectangular slabs on elastic foundations; however, the stability equations were different for the various combinations of classical boundary conditions, which complicates their implementation. Even though there are procedures to analyze the stability of beam-columns on an elastic foundation with generalized boundary conditions (Areiza-Hurtado et al., 2005), no such expressions exist for rigid pavements.

Rigid-pavement blowup can be understood by studying the stability of slabs on an elastic foundation (also known as a liquid, or Winkler, foundation). Rigid pavements contract during cold temperatures, increasing the joint spacing. The space between slabs can potentially be filled with incompressible debris, constraining pavement expansion during high temperatures. Restrained expansion translates into axial forces in the concrete slab, which might increase until reaching a buckling load. Some attempts have been made to give theoretical explanation to pavement blowup, mainly by Kerr and his coauthors (Kerr, 1994, 1997; Kerr & Dallis, 1985; Kerr & Shade, 1984). The work revolved around determining safe temperature increments before the rigid pavement buckled, and it assumed uniform temperature increment. A long pavement was considered, and the analysis was performed on a unit-width slab supported on an infinitely rigid base. In addition, nonlinear pavement-base shear interface forces were included (Kerr & Dallis, 1985; Kerr & Shade, 1984). The solution was used to determine the relevance of various variables on rigid-pavement stability, such as the coefficient of thermal expansion, pavement thickness and stiffness, pavement base interface forces, and stiffness at joints and cracks (Kerr and Dallis, 1985). The methodology was extended to quantify the influence of an adjacent rigid structure on pavement blowup (Kerr, 1994). The main drawback of this work lies in assuming a long pavement and an infinitely rigid base support.

3. SLAB-ON-GRADE RIGID PAVEMENT

Closed-form expressions for calculating stresses and displacements of partially restrained concrete pavement caused by a linear temperature gradient are presented in this section. Translational and rotational linear elastic springs along the slab edges defined the partial restraint. In addition to plate theory behavior, the model assumes linear elastic concrete and an infinitely long slab resting on a Winkler foundation. The solutions of curling stresses and displacements were validated using the FE method and quantified the effects of semirigid connections, slab and foundation material properties, and slab thickness and width. Rotational and translational restraints, which can be related to joint condition in concrete pavement, had significant influence on the magnitude and location of maximum curling stresses and deflections. In addition, Westergaard's analysis, a particular case of the proposed solution when there is no restriction along the slab's edges, resulted in the largest deflections at the center of the slab and the lowest maximum curling stresses. Adjustment factors that convert the theoretical findings from an infinitely long slab to a square slab are proposed.

3.1 STRUCTURAL MODEL, DEFLECTIONS, AND CURLING STRESSES

Consider a slab extending to infinity along the *x*-direction, with width *b* along the *y*-direction, and thickness *h*, as shown in figure 1. The slab is made of linear elastic material with elastic modulus *E*, Poisson's ration *v*, and coefficient of thermal expansion *α*. The plate is supported by an elastic foundation with modulus of subgrade reaction *k* that does not allow separation. Furthermore, the slab is subjected to a linear temperature gradient, where the difference in temperature between the slab's top and bottom is *ΔT*.

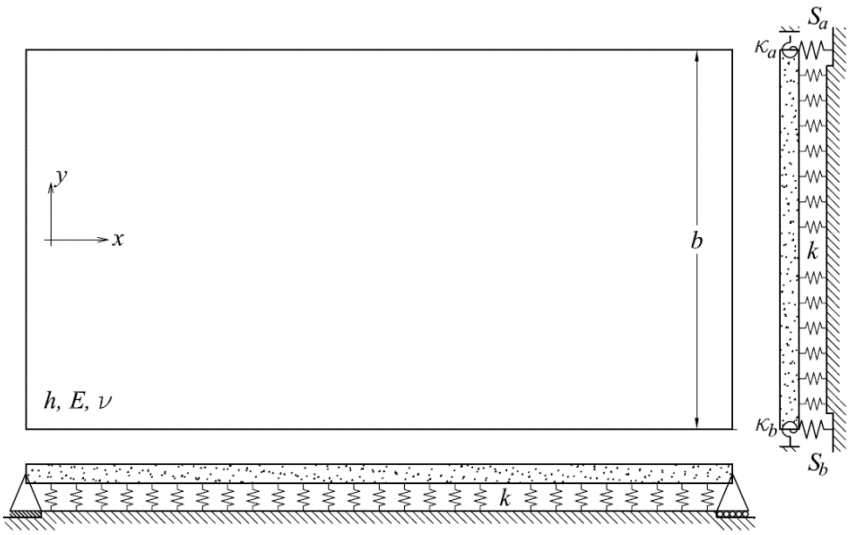

Figure 1. Partially Restrained Infinitely Long Slab

The vertical displacement and rotation along the edges parallel to the x-axis are restrained by linear elastic springs. Along the edge $y = b/2$, the translational and rotational linear springs have a magnitude per unit length of S_a and κ_a, respectively. Similarly, S_b and κ_b are the rotational and translational springs per unit length along the edge $y = -b/2$. Elastic constraints have the advantage of capturing the classical boundary condition. For instance, if S_a, κ_a, S_b, and κ_b are zero, there is no restriction to movement, and the edges are free. Conversely, if the magnitude of the springs is very high, the edges are fully restrained, so they are clamped. Finally, if the edges are free to rotate and cannot displace, they are pinned.

Assuming that the slab's cross section before and after bending is a plane, h is small compared to the other dimensions, and vertical strain is negligible, it can be found that for an infinitely long slab subjected to a linear temperature gradient, the bending moment with respect to the y-axis is the following (Timoshenko & Woinowsky-Krieger, 1959; Westergaard, 1927):

$$M_y = -\frac{Eh^3}{12(1-\nu^2)}\left[\frac{d^2w}{dy^2} + \frac{1+\nu}{h}\Delta T\right] \tag{1}$$

The equilibrium of a differential element in the slab provides $d^2M_y/dy^2 = kz$, so the differential equation for the vertical deflection is as follows:

$$l^4 \frac{d^4 w}{dy^4} + w = 0 \tag{2}$$

where $l = \sqrt[4]{D/k}$ is the radius of relative stiffness and $D = Eh^3/12/(1-\nu^2)$ is the slab's bending stiffness. Equations 1 and 2 were used by Westergaard (1927). The shear and bending moment per unit length along the partially restrained edges of the slab are as follows:

$$V\left(\frac{b}{2}\right) = -S_a w\left(\frac{b}{2}\right) \tag{3}$$

$$V\left(-\frac{b}{2}\right) = S_b w\left(-\frac{b}{2}\right) \tag{4}$$

$$M\left(\frac{b}{2}\right) = \kappa_a \theta\left(\frac{b}{2}\right) \tag{5}$$

$$M\left(-\frac{b}{2}\right) = -\kappa_a \theta\left(-\frac{b}{2}\right) \tag{6}$$

The general solution of equation 2 is

$$\begin{aligned} w(y) = {} & C_1 \cosh\left(\frac{y}{l\sqrt{2}}\right)\cos\left(\frac{y}{l\sqrt{2}}\right) \\ & + C_2 \cosh\left(\frac{y}{l\sqrt{2}}\right)\sin\left(\frac{y}{l\sqrt{2}}\right) + C_3 \sinh\left(\frac{y}{l\sqrt{2}}\right)\cos\left(\frac{y}{l\sqrt{2}}\right) \\ & + C_4 \sinh\left(\frac{y}{l\sqrt{2}}\right)\sin\left(\frac{y}{l\sqrt{2}}\right) \end{aligned} \tag{7}$$

where C_1, C_2, C_3, and C_4 are constants found by solving the linear system of equations resulting from substituting $w(y)$ from equation 7 into the boundary conditions in equations 3-6. The solution for the slab's vertical displacement is as follows:

$$\begin{aligned} w(y) = {} & \frac{1}{Det(A)} \frac{(1+\nu)\alpha\Delta T}{h} l^2 \left[c_1 \cosh\left(\frac{l}{\sqrt{2}}\right)\cos\left(\frac{l}{\sqrt{2}}\right) \right. \\ & + c_2 \cosh\left(\frac{l}{\sqrt{2}}\right)\sin\left(\frac{l}{\sqrt{2}}\right) + c_3 \sinh\left(\frac{l}{\sqrt{2}}\right)\cos\left(\frac{l}{\sqrt{2}}\right) \\ & \left. + c_4 \sinh\left(\frac{l}{\sqrt{2}}\right)\sin\left(\frac{l}{\sqrt{2}}\right) \right] \end{aligned} \tag{8}$$

Appendix A presents the system of equations, its solution, and the expressions for c_1, c_2, c_3, c_4, and $Det(A)$ as a function of $R_a = \kappa_a l/D$, $R_b = \kappa_b l/D$, $T_a = S_a l^3/D$, and $T_b = S_b l^3/D$. Once deflection is calculated, rotation, curvature, bending moment M_y from equation 1, shear force, and stresses on top of the slab $\sigma_y = 6M_y/h^2$ can also be computed using the deflection $w(y)$. The stresses in the y-direction are as follows:

$$\sigma_y\,(y) = -\frac{E\alpha\,\Delta T}{2(1-\nu)}\left[1-\frac{1}{Det(A)}\left(c_1\sin\left(\frac{l}{\sqrt{2}}\right)\sinh\left(\frac{l}{\sqrt{2}}\right)\right.\right.$$
$$-\ c_2\cos\left(\frac{l}{\sqrt{2}}\right)\sinh\left(\frac{l}{\sqrt{2}}\right)+c_3\cosh\left(\frac{l}{\sqrt{2}}\right)\sin\left(\frac{l}{\sqrt{2}}\right) \quad (9)$$
$$\left.\left.-\,c_4\cos\left(\frac{l}{\sqrt{2}}\right)\cosh\left(\frac{l}{\sqrt{2}}\right)\right)\right]$$

In the case studied by Westergaard (1927), the infinitely long slab is free to displace and rotate along its edges (i.e., R_a=R_b=T_a=T_b=0). Consequently, using the formulae in appendix A:

$$\frac{c_1}{Det(A)} = 2\cosh\lambda\frac{\sin\lambda\ -\cos\lambda\tanh\lambda}{\sinh 2\lambda+\cos 2\lambda} \quad (10)$$

$$\frac{c_2}{Det(A)} = 0 \quad (11)$$

$$\frac{c_3}{Det(A)} = 0 \quad (12)$$

$$\frac{c_4}{Det(A)} = -2\cosh\lambda\frac{\sin\lambda+\cos\lambda\tanh\lambda}{\sinh 2\lambda+\cos 2\lambda} \quad (13)$$

So, the displacement becomes

$$w(y) = \alpha\Delta T\,(1$$
$$+\nu)\ \frac{l^2}{h}\frac{2\cosh\lambda}{\sinh 2\lambda+\cos 2\lambda}\left[(\sin\lambda\right.$$
$$-\cos\lambda\ \tanh\lambda)\cosh\frac{y}{l\sqrt{2}}\cos\frac{y}{l\sqrt{2}} \quad (14)$$
$$\left.-(\sin\lambda+\cos\lambda\ \tanh\lambda)\sinh\frac{y}{l\sqrt{2}}\sin\frac{y}{l\sqrt{2}}\right]$$

which can be reduced to

$$w(y) = -\alpha\Delta T\,(1+\nu)\ \frac{l^2}{h}\frac{2\cosh\lambda\cos\lambda}{\sinh 2\lambda+\cos 2\lambda}\left[(-\tan\lambda+\tanh\lambda)\cosh\frac{y}{l\sqrt{2}}\cos\frac{y}{l\sqrt{2}}\right.$$
$$\left.+\,(\tan\lambda+\tanh\lambda)\sinh\frac{y}{l\sqrt{2}}\sin\frac{y}{l\sqrt{2}}\right] \quad (15)$$

Equation 15 matches the one reported by Westergaard (1927).

3.2 EXAMPLE

A typical rigid pavement is used to demonstrate the applicability and validity of the proposed solution. The concrete slab has elastic modulus E=28 MPa, coefficient of thermal expansion

α=9×10^(-6) 1/°C, and Poisson's ratio ν=0.15. The slab rests on an elastic foundation with modulus of subgrade reaction k=0.0542 N/mm3; the slab's thickness and width are h=200 mm and b= 4.0 m, respectively. The dowel bars have diameter and spacing of 31.8 and 305 mm, respectively. The dowel bars are made of steel with an elastic modulus of 200 GPa and a Poisson's ratio of 0.30. In addition, the width of the joint is 6.35 mm; and the dowel-concrete interaction coefficient is 407.3 N/mm3 (Guo et al., 1995). The temperature on top of the slab is 10°C lower than that at the bottom. The objective is to calculate the deflection and curling stresses of the slab, assuming that (1) edges are free to rotate and displace (Westergaard case); and (2) one edge is elastically restrained as to rotation and translation with the dowel configuration described above, and the other edge adjoins a bridge abutment that provides no restriction to rotation or translation.

The elastic constraint provided by the dowel system was calculated following the procedure proposed by Guo et al. (1995). The procedure calculates a stiffness matrix by dividing the dowel in three segments, two inside the concrete and one spanning the joint's width. The stiffness matrix is given by the following:

$$\boldsymbol{S_c} = \begin{bmatrix} \boldsymbol{T_1} & 0 \\ 0 & \boldsymbol{T_2} \end{bmatrix} \left(\begin{bmatrix} \boldsymbol{I} & 0 \\ 0 & I \end{bmatrix} - \begin{bmatrix} \boldsymbol{K_{11}} + \boldsymbol{T_1} & \boldsymbol{K_{12}} \\ \boldsymbol{K_{21}} & \boldsymbol{K_{22}} + \boldsymbol{T_2} \end{bmatrix}^{-1} \begin{bmatrix} \boldsymbol{T_1} & 0 \\ 0 & \boldsymbol{T_2} \end{bmatrix} \right) \tag{16}$$

where:

$$\boldsymbol{T_1} = \frac{2\beta^2 E_d I}{C_1^2 + c_1^2} \begin{bmatrix} 2\beta(S_1 C_1 + s_1 c_1) & -(S_1^2 + s_1^2) \\ -(S_1^2 + s_1^2) & \dfrac{S_1 C_1 - s_1 c_1}{\beta} \end{bmatrix} \tag{17}$$

$$\boldsymbol{T_2} = \frac{2\beta^2 E_d I}{C_2^2 + c_2^2} \begin{bmatrix} 2\beta(S_2 C_2 + s_2 c_2) & S_2^2 + s_2^2 \\ S_2^2 + s_2^2 & \dfrac{S_2 C_2 - s_2 c_2}{\beta} \end{bmatrix} \tag{18}$$

with $S = \sinh \beta L$, $C = \cosh \beta L$, $s = \sin \beta L$, and $c = \cos \beta L$. Subscripts 1 and 2 represent the left and right segments, respectively, of the dowel bar that is embedded in the concrete; and L corresponds to the distance that is embedded in the slab. In addition, $\beta = [k_b/(4E_d I)]^{0.25}$; k_b is the product of the dowel-concrete interaction coefficient and the dowel diameter, E_d is the elastic modulus of the dowel bar, and I is the dowel bar's moment of inertia. For the dowel characteristics in this example, β =23.86 1/m.

The terms K_{11}, K_{12}, K_{21}, and K_{22} are defined by the segment of the dowel bar between slabs, as follows:

$$\boldsymbol{T_1} = \begin{bmatrix} K_{11} & K_{12} \\ K_{21} & K_{22} \end{bmatrix} = \frac{E_d I}{l^3(1+\phi)} \begin{bmatrix} 12 & 6l_{db} & -12 & 6l_{db} \\ 6l_{db} & (4+\phi)l_{db}^2 & -6l_{db} & (2-\phi)l_{db}^2 \\ -12 & -6l_{db} & 12 & -6l_{db} \\ 6l_{db} & (2-\phi)l_{db}^2 & -6l_{db} & (4+\phi)l_{db}^2 \end{bmatrix} \tag{19}$$

where l_{db} is the length of the bar between slabs (i.e., the width of the joint), $\phi = 12E_d I/(GA_s l^2)$, and A_s is the dowel's cross-sectional area effective in shear. After replacing all the variables, the stiffness matrix (force in kN and distance in m) is as follows:

$$\boldsymbol{S_c} = \begin{bmatrix} 11023.2 & -194.8 & -11023.2 & 264.8 \\ -194.8 & 8.4 & 194.8 & -9.6 \\ -11023.2 & 194.8 & 11023.2 & -264.8 \\ 264.8 & -9.6 & -264.8 & 11.3 \end{bmatrix} \tag{20}$$

The translational and rotational restraints per unit distance are obtained by dividing entries 11 and 22 by the dowel-bar spacing: S_a=11023.3/0.305=36.1 N/mm/mm, and κ_a=8.4/0.305=27533.1 N.mm/mm/rad.

An FE model with the same characteristics was created in the ABAQUS software (ABAQUS, 2014). A slab three times longer than its width (i.e., 12.0-m long) represented infinite length. The model used square shell elements with a 32-mm side, four nodes, and Gauss quadrature for section integration. Elastic connectors with constants obtained by multiplying the magnitude per unit length and the length of the shell elements represented the elastic restraints. For instance, for the translational spring along edge a, S_a=36.1 N×mm/mm, so the input for ABAQUS is 36.1 N×mm/mm×32.0 mm = 1156.5 N/mm. The foundation element modeled the Winkler foundation, and the linear temperature variation was specified using the temperature gradient through the slab thickness (0.05 °C/mm).

The agreement between the proposed closed-form solution and the FE model is excellent, as is shown in figure 2. The figure presents the variation of the deflection and the curling stresses obtained from equations 8 and 9, respectively. The horizontal axis indicates the slab's width, with y=0 being the slab's center, and the vertical axis representing the vertical deflection and curling stresses for top and bottom plots, respectively. The match was slightly better for deflection than for stresses. For instance, at the center of the slab, the differences in deflection for the free and the partially restrained slab were 3.1% and 2.7%, respectively. In contrast, the difference in stress was 5.5% for the free slab, and 4.4% for the slab with semirigid connections.

Asymmetrical behavior for the partially restrained slab can also be inferred from figure 2. Unequal semirigid connections along the slab's edges caused the asymmetry. The maximum response is not at the center anymore, as for the free slab. On the contrary, the maximum is at y=247.6 mm for deflection and y=158.7 mm for curling stresses. The critical curling stresses increased by 13% for the elastically restrained slab, as compared to the Westergaard case. Similarly, curling stresses were equal to zero at the free edges; but they were neither zero nor equal for the elastically restrained slab. In fact, the curling stress is -0.974 MPa along edge a (i.e., y=2.0 m) and -0.753 MPa along edge b (i.e., y=-2.0 m).

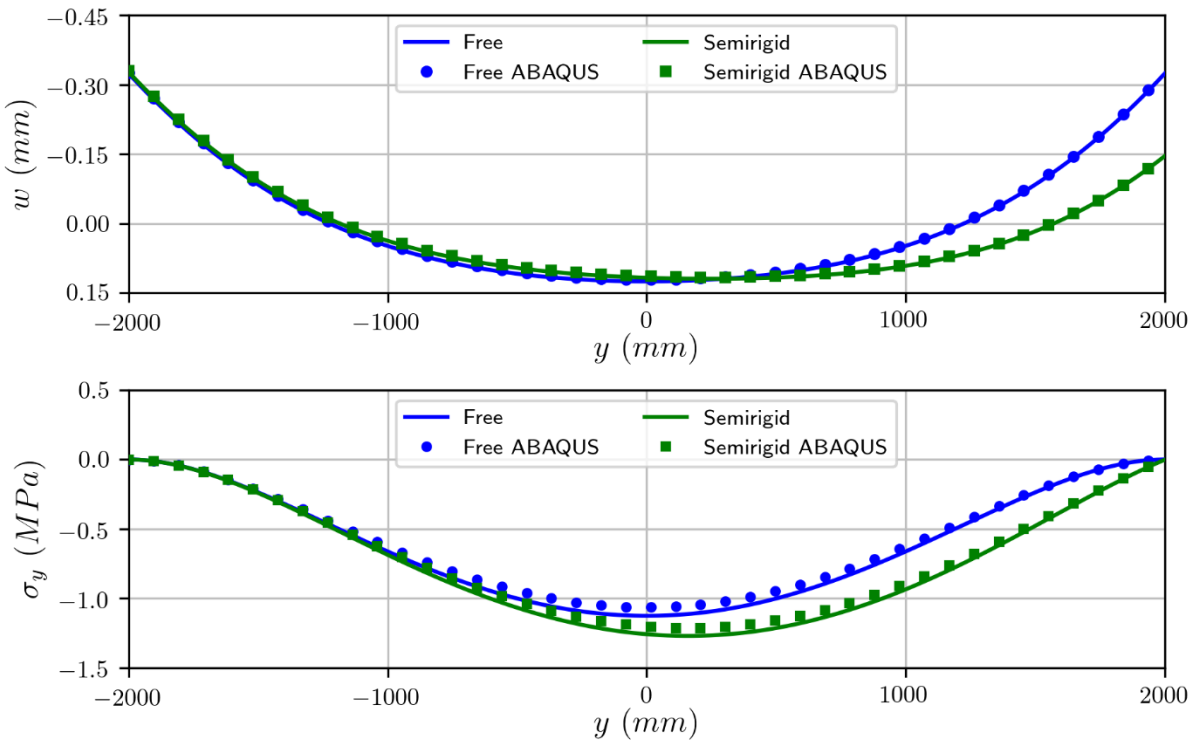

Figure 2. Comparison Between Proposed Equations and ABAQUS

Transitioning from a free to an elastically restrained slab affects the magnitude and variation of curling stresses and deflections along the slab's width. The following section elaborates on the effect of semirigid connection on curling stresses and deflections for a broad range of scenarios.

3.3 EFFECT OF SEMIGRID CONNECTIONS

A parametric study was performed to evaluate the importance of the semirigid connections on curling stresses and deflections. The analyzed cases included 36 combinations of rotational and translational semirigid connections at edges a and b for a fixed ratio between the slab's width and radius of relative stiffness. The ratio was b/l = 5, which is recommended by design procedures to reduce the likelihood of transverse cracking (Federal Highway Administration (FHWA), 1990). The restraint parameters—R_a, R_b, T_a, and T_b—were 0, 1, and 100 each, respectively; R_a=0 represents no restriction to rotation along edge a, while R_b=100 indicates full restriction. Theoretically, full restriction is given by R_a=∞, but preliminary analysis showed that the difference between R_a =100 and R_a=∞ is insignificant.

3.3.1 Deflection

Figure 3 presents the deflection across the slab's width for various combinations of boundary conditions. The vertical axis shows the normalized deflection $\bar{w} = w/w_o$ with $w_o = \alpha\Delta T(1+\nu)l^2/h$; the horizontal axis is the position along the slab's width normalized with respect to the width, $\bar{y} = y/b$. The normalized parameters for the translational restriction are fixed

in each subplot, and the six lines correspond to different combinations of the normalized parameters for rotational restriction.

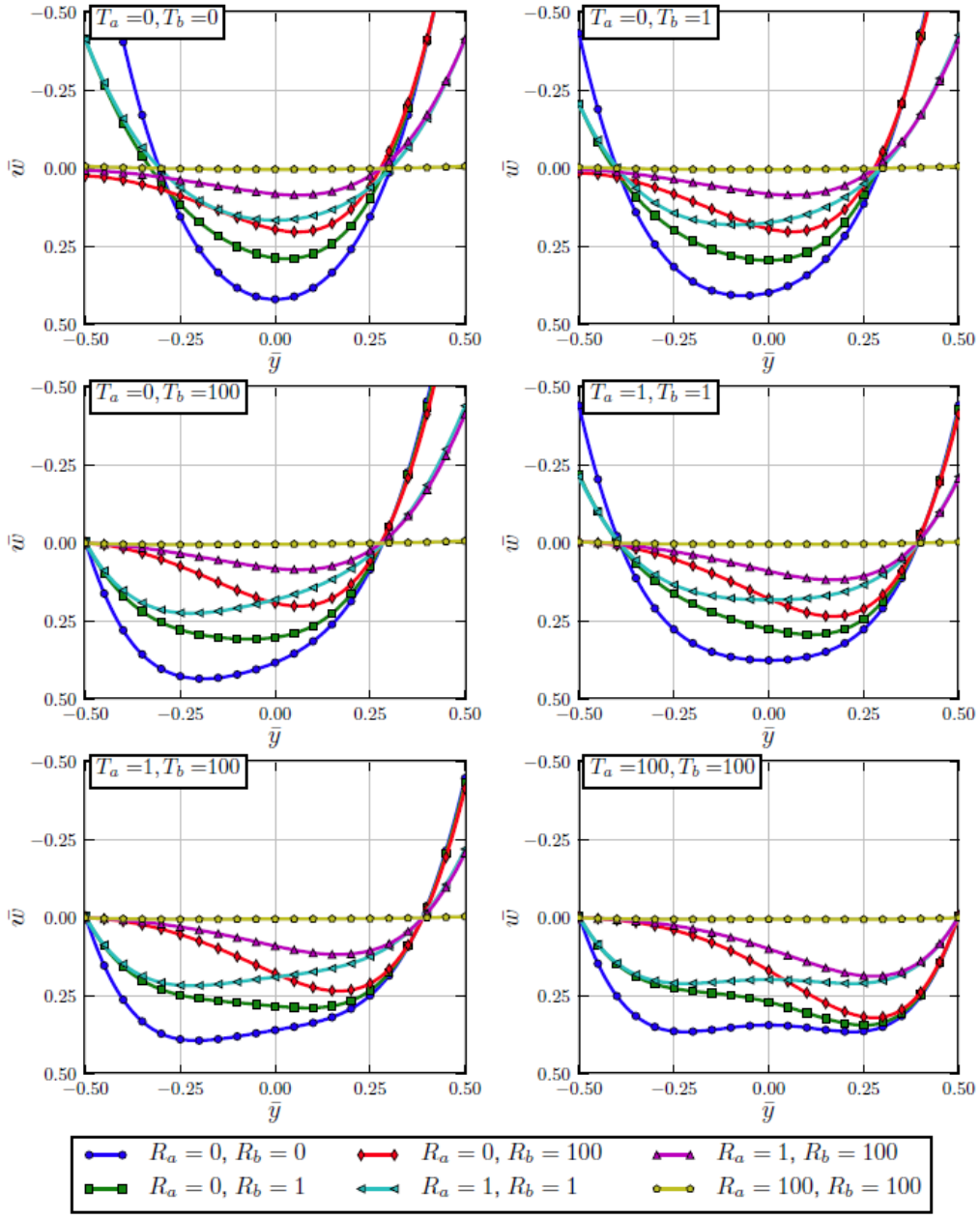

Figure 3. Effect of Semirigid Connections on Slab's Deflection

Rotational springs affected vertical deflection around the slab's center more than did translation springs. On one hand, deflection was always zero when R_a=R_b=100 regardless of the degree of translational restraint. On the other hand, no restriction to rotation resulted in the highest deflection around the center of the slab. As degree of rotational restriction increased, deflection gradually changed from the maximum value to zero. This result can be proved by comparing $\overline{w}$ at the center of the slab for three cases. First, the normalized deflection is 0.419 when T_a=T_b=R_a=R_b=0

(Westergaard case). Second, if the normalized rotational springs are changed to R_a=0 and R_b=100, $\bar{w}$ becomes 0.195, which is a 53% reduction. Third, if the rotational springs are maintained at zero, and T_a=0 and T_b=100, the normalized deflection is 0.382, a decrement of only 8.8%, as compared to the Westergaard case. These results are the consequence of bending being the main deformation mechanism of slabs.

Even though translational springs were less relevant than rotational ones for deflection, the difference between T_a and T_b determines if Westergaard's solution is conservative. As mentioned above, maximum $\bar{w}$ for free edges was 0.419. The magnitude of $\bar{w}$ for the free case is smaller than 0.434, which corresponds to T_a=0 and T_b=100 (highest difference between translational springs). However, if T_a=100 and T_b=100, then $\bar{w}$=0.365, which is smaller than that for the free case. Consequently, regarding deflection, Westergaard is more conservative if there is high translational restriction at the edges of the slab; but it is not conservative if the difference between T_a and T_b is large.

Semirigid connection also affects the location of maximum deflection. As would be expected, the largest deflection occurred at the center of the slab only if the boundary conditions were symmetric (i.e., R_a=R_b and T_a=T_b). The difference between deflection at the center and maximum deflection can be significant. The highest ratio between maximum deflection and deflection at the center was 1.89 for T_a=100, T_b=100, R_a=0, and R_b=100. The difference between the normalized rotational springs was the controlling factor for the discrepancy between maximum deflection and deflection of the slab's center.

3.3.2 Curling Stresses

Figure 4 presents the curling stresses along the slab's width. As for deflection, the horizontal axis is the ratio between the transverse location and the slab's width. The vertical axis indicates the stresses normalized with respect to the stress for a fully restrained slab $\sigma_o = E\alpha\,\Delta T/2/(1-\nu)$. The arrangement of the plots regarding the semirigid connections is the same as in figure 3.

Figure 4 confirms the expected behavior for extreme values of R_a and R_b. First, whenever the rotational restrictions were zero (i.e., R_a=0 or R_b=0), the curling stresses along the corresponding edge were zero. On the contrary, if the restriction along both edges is high (i.e., R_a=100 and R_b=100), the curvature of the slab is unchanged, so the stresses were constant and equal to $E\alpha\Delta T/2/(1-\nu)$, as indicated by $\bar{\sigma}$=1. The result holds for any combination of translational springs because the deflection is zero when R_a=R_b=100 regardless of T_a and T_b.

The ratio $\bar{\sigma}$ along the edges was affected differently by the translational and rotational connections. As the translational restraint increased, the ratio decreased. For instance, for R_a=0 and R_b=1, if T_a=T_b=0, $\bar{\sigma}$=0.631 at y/b=-0.50. In contrast, if T_a is kept at zero and T_b is increased to 1, the ratio decreases by 14% to 0.545. The curling-stress ratio would decrease an extra 16% to 0.462 if T_b changes from 1 to 100. On the contrary, as the degree of rotational restriction increased, $\bar{\sigma}$ would be raised as well. If T_a=T_b=1, $\bar{\sigma}$=0.532 at edge $-b/2$ when R_a=0 and R_b=1, which is higher than the ratio when the edge is free to rotate ($\bar{\sigma}$=0 when R_a=R_b=0) and smaller than when the edge is fully restrained as to rotation ($\bar{\sigma}$=1.05 when R_a=0 and R_b=100).

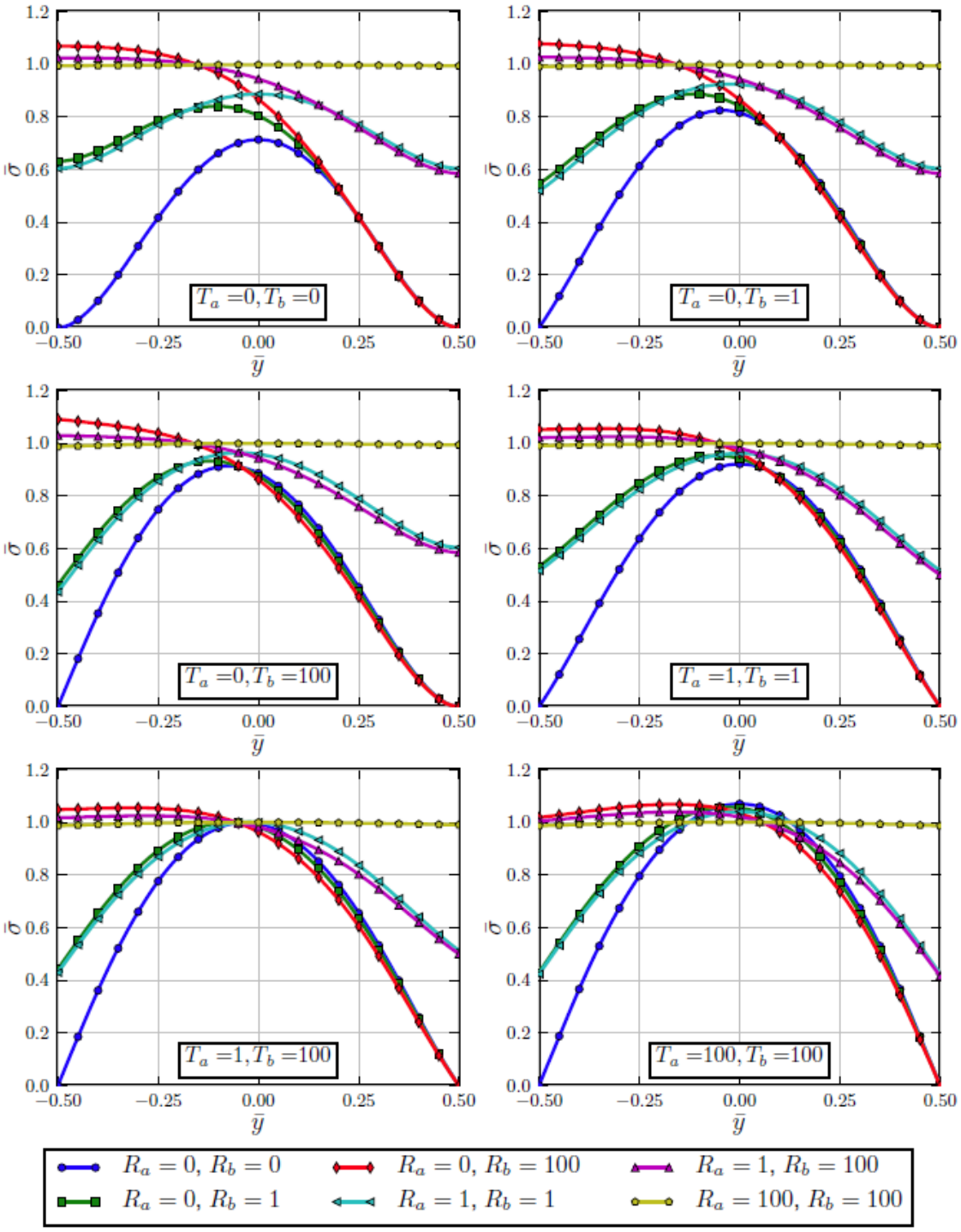

Figure 4. Effect of Semirigid Connections on Stresses

The variation of the curling stresses with respect to semirigid connections along the center of the slab is different than along the edges. Considering the same cases as in the previous paragraphs, for R_a=0 and R_b=0, if T_a=T_b=0, $\bar{\sigma}$=0.713 at y/b=0. The ratio is raised to 0.816 if the dimensionless translational spring along edge a is maintained at 0 and increased to 1 along edge $-b/2$. If T_b is

raised to 100 and T_a=0, $\bar{\sigma}$=0.886. In other words, when both edges are free to rotate, curling stresses at the center of the slab increase 24% between free and full-translational restraint; and most of the increment occurs between T_b=0 and T_b=1. Taking Westergaard's case as a reference, the influence of rotational springs can also be inferred. If T_a and T_b are kept at zero, $\bar{\sigma}$ changes from 0.713 to 0.804 if R_b is changed from 0 to 1 and R_a=0 is held constant (13% increment). In addition, if R_b becomes 100, the ratio increases by 8% to 0.867. In general, the influence of rotational and translational springs on curling stresses at the center of the slab decreases as the edge restrictions became greater.

From a practical perspective, the observations above highlight the relevance of properly characterizing the load-transfer efficiency when calculating curling stresses, not only of the shear force but also of the bending moment between concrete slabs. The Westergaard case predicts the lowest curling stresses, which means the free-edge assumption is not conservative and can result in premature deterioration of concrete pavements.

3.4 CURLING STRESSES AND *b/L* RATIO

The influence of semirigid connections on curling stresses also depends on geometry and material properties. These variables are encompassed in the ratio b/l, which depends not only on the slab's thickness, width, and material properties, but also on the modulus of subgrade reaction. In addition, design guidelines recommend limiting b/l to 5 to reduce transverse cracking (FHWA, 1990). Figure 5 shows the relevance of b/l on curling stresses; it shows the variation of the normalized maximum curling stress $\bar{\sigma}_{max} = \sigma_{max} / \sigma_o$ for a wide range of b/l and the same values of the semirigid connections as in figures 3 and 4.

Large b/l ratios suggest the smallest effect of boundary conditions on curling stresses. For every combination of T_a and T_b, the largest $\bar{\sigma}_{max}$ at b/l=10 was found for R_a=R_b=100. Specifically, when R_a=R_b=100 and T_a=T_b=0, the maximum curling stresses are 6.6% higher than σ_o. Large b/l represents very long slabs, where the maximum curling stresses are obtained by assuming full restriction at the edges, thus explaining the minimal effect of boundary conditions on $\bar{\sigma}_{max}$.

In general, as the degree of translational restriction increased, $\bar{\sigma}_{max}$ raised and the corresponding b/l decreased. For instance, if T_a is fixed at zero and T_b is changed among 0, 1, and 100, the ratio between the maximum curling stress and σ_o is 1.079, 1.127, and 1.240, respectively. Furthermore, the value of b/l at each maximum decreased: b/l=4.45 for $\bar{\sigma}_{max}$=1.079, b/l=3.90 for $\bar{\sigma}_{max}$=1.127, and b/l=3.35 for $\bar{\sigma}_{max}$=1.240. The highest ratio, $\bar{\sigma}_{max}$=1.431, requires three conditions: T_a=T_b=100, the difference between rotational springs at both edges was the highest (R_a=0 and R_b=100), and b/l=1.65. In summary, special attention should be given to load-transfer-efficiency assessment when calculating curling stresses of short slabs. The only case with no influence of translational restriction on $\bar{\sigma}_{max}$ is when edge rotation is fully restrained (i.e., R_a=R_b=100), in which case the ratio is one.

Edge conditions where rotation and/or displacement are either free or fully restrained can result in under- or overprediction of $\bar{\sigma}_{max}$, depending on the magnitude of b/l. The b/l changes with T_a and T_b, being the highest for T_a=T_b=0, and the lowest for T_a=T_b=100. Similarly, if rotation is fully restrained (i.e., R_a=R_b=100), three ranges were identified. First, if b/l was sufficiently small, $\bar{\sigma}_{max}$

was the highest among all values of R_a and R_b. Second, for intermediate b/l, $\bar{\sigma}_{max}$ was higher than any case with one edge not fully restrained as to rotation. Third, for high b/l magnitudes, full rotational restriction provided the smallest $\bar{\sigma}_{max}$.

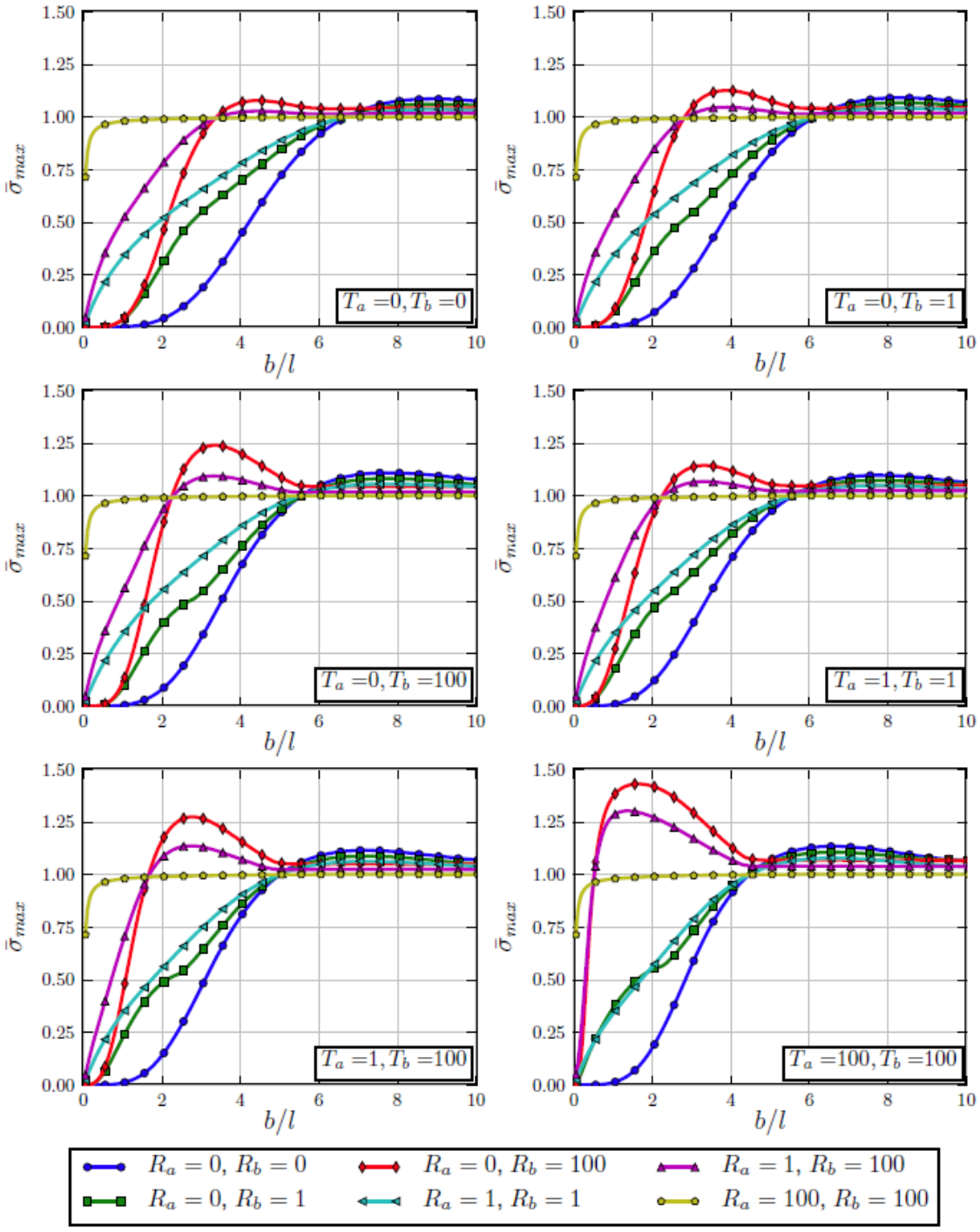

Figure 5. Effect of Ratio Between a Slab's Width and Radius of Relative Stiffness on Maximum Stresses

Even though design guidelines restrict b/l to 5, the effect of the rotational springs on the normalized maximum curling stress is highly sensitive to the ratio between the slab's width and the radius of relative stiffness if b/l< 5. For instance, if T_a=T_b=1 and b/l =3.5, the maximum and minimum $\bar{\sigma}_{max}$ are 1.143 and 0.546, respectively, a difference of 0.597. If b/l is changed to 4.0, the maximum is 1.120, and the minimum changes to 0.679, which represents a difference of 0.441, 27% smaller than for b/l =3.5.

3.5 ADJUSTMENT FACTOR FOR SQUARE SLAB

Because the presented solution assumes an infinitely long slab, an adjustment factor (AF) is proposed to modify the maximum stresses for a square slab. First, the maximum curling stress for the infinitely long slab was calculated using equation 9, while for the square slab it was obtained using the FE model. AF is defined as the ratio between the maximum curling stress of the square slab over the one calculated using equation 9. AF was calculated for 720 cases that resulted from the combination of (1) six rotational springs pairs (R_a=0 – R_b=0, R_a=0 – R_b=1, R_a=0 – R_b=100, R_a=1 – R_b=1, R_a=1 – R_b=100, and R_a=100 – R_b=100); (2) six translational spring pairs (T_a=0 – T_b=0, T_a=0 – T_b=1, T_a=0 – T_b=100, T_a=1 – T_b=1, T_a=1 – T_b =100, and T_a=100 – T_b=100); (3) four moduli of subgrade reaction (k=0.01, 0.05, 0.1, and 0.02 N/mm^3); and (4) five thicknesses (h=100, 200, 300, 400, and 500 mm). Figure 6 presents the variation of AF with b/l.

Two zones can be distinguished when analyzing the effect of b/l on AF. First, as expected, the wider the slab (large b/l) the smaller the difference between square and infinite geometries. AF for relatively large b/l is not exactly one due to numerical differences between the FE and the analytical solution. It is also noted that $AF \approx 1$ requires a significant b/l, approximately 7 or larger. Second, AF has a wide variation when b/l<7, where AF can reach values higher than 2 and as low as zero.

Considering the case b/l=5, which is recommended in rigid-pavement design, three main observations can be made. First, for all combinations of T_a and T_b, the effect of rotational springs can be divided into two groups: when R_b = 100, AF is high; and when $R_b \neq 100$, AF is low. Second, the smallest quotient between the minimum and maximum AF is 1.11 when T_a =T_b=0. Third, the slab fully restrained against translation (i.e., T_a =T_b=100) results in the largest change in AF; it is 0.35, a 42% increment.

The influence of rotational and translational springs on AF is interconnected. As explained, for b/l =5, the lines corresponding to R_b=100 tended to be close for all T_a–T_b combinations; however, the lines did not always represent high AF, mainly for low b/l. Changes in translational springs are associated with changes in the magnitude of the lines, while variations of the rotational springs change the shape of the lines. Figure 6 also shows that the only case providing adjustment factors smaller than one is when R_a=R_b=0. Hence, the infinite slab always provides smaller values than the square one if slab edges are free to rotate. In general, whether or not the infinite-slab assumption is conservative depends on b/l and the semirigid connections.

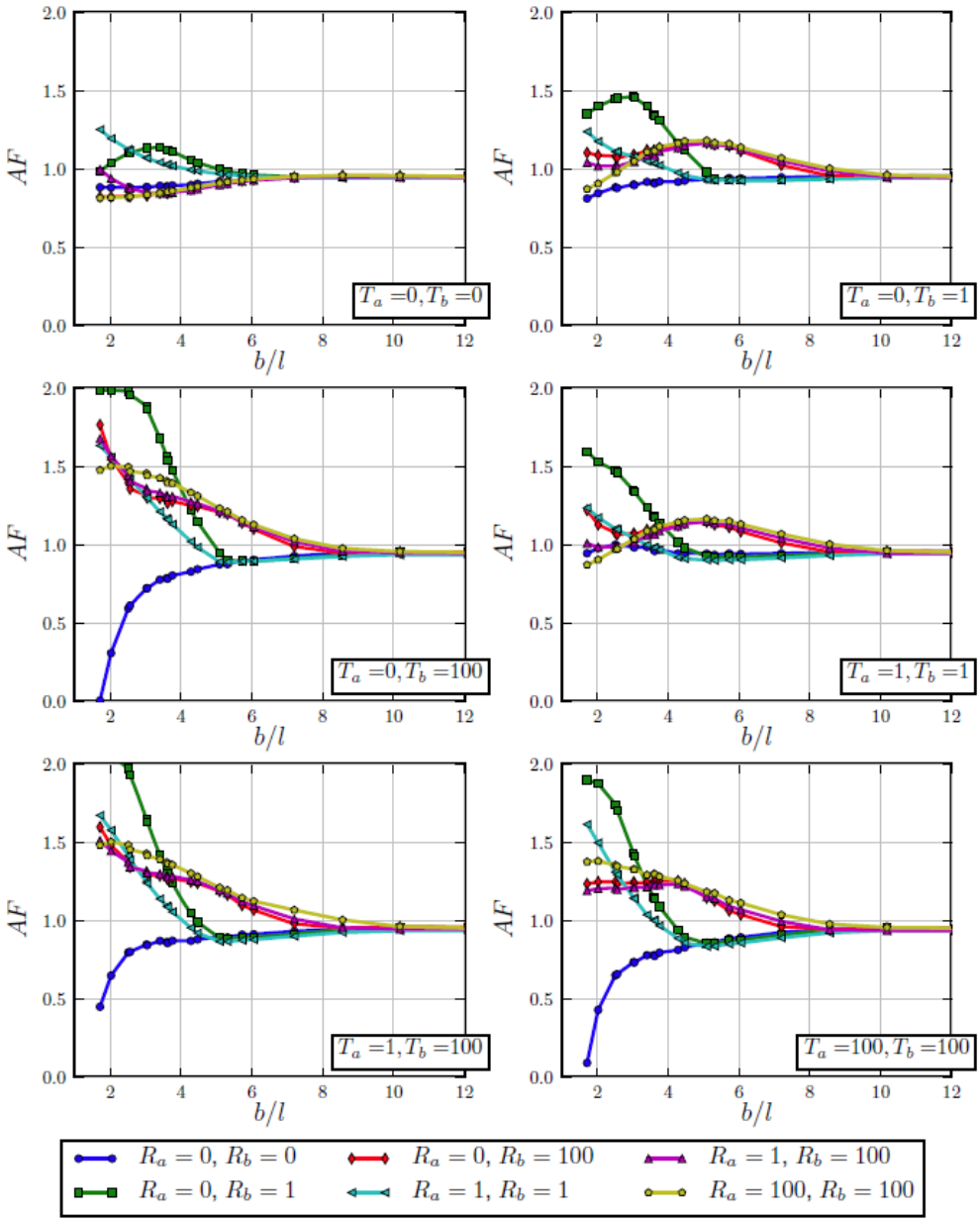

Figure 6. Effect of Semirigid Connections on Adjustment Factor for Square Slab

3.6 SUMMARY

A closed-form solution for curling responses of slab-on-subgrade rigid pavement considering generalized boundary conditions was derived using plate theory. The derivation adopted the assumptions of the classical work of Westergaard except for the condition of the slab's edges, which were partially restrained as to displacement and rotation by linear elastic springs. After validation of the solution using the FE method, the equations quantified the effect of edge restrictions on curling stresses and displacements for a wide range of material properties and geometries. To implement the closed-form solution to real-life cases, adjustment factors were calculated to link curling stresses of an infinitely long slab and a square slab.

Comparison with the FE method showed a difference of approximately 5% for stresses and displacements, with slightly better agreement for displacements. It was found that the elastic restraints affect the magnitude and location of maximum deflection, with rotational springs having more influence than translational ones at the slab's center. In addition, for small ratios between the slab's width and radius of relative stiffness, semirigid conditions greatly affect the quotient between the maximum curling stresses and the curling stresses of a fully restrained slab. Finally, maximum curling stresses in square slabs are usually higher than those for an infinitely long slab; the difference heavily depended on the boundary conditions and b/l ratio. This study also presents an adjustment factor for the currently used approach to analyze maximum curling stresses in rigid pavement with square slabs.

The results show that Westergaard analysis is not conservative, and that the degree of relevance of the semirigid connections depends on material properties and geometry. More generally, when performing curling analysis, it is imperative to assess and quantify the joints' condition and their ability to transfer shear force and bending moment.

4. JOINT ROTATION AND CURLING RESPONSES IN AIRFIELD RIGID PAVEMENT

This section quantifies the relevance of restriction to joint rotation of an airfield concrete pavement when calculating critical curling stresses and deflections using a validated FE model. The validation used strains measured at the John F. Kennedy International Airport (JFK). To calculate critical curling stresses and deflections, the pavement was subjected to 5,263 hours of temperature as determined by utilizing the EICM and thermocouple readings. The profiles included a wide range of average temperatures, temperature gradients, and temperature nonlinearity. Three conditions were included: (1) joints free to displace and rotate, (2) joints free to rotate but partially restrained as to vertical displacement, and (3) joints partially restrained as to vertical displacement and rotation. The differences in critical stresses between the second and third conditions were higher than 5% in 70% of the hours. In addition, critical deflections were lower when considering the rotational restriction; 80% of the difference with respect to the free case was caused by rotational restriction. As a conclusion, joint rotation intensifies the influence of curling stresses and deflections on long-term performance of airfield rigid pavement.

4.1 FINITE ELEMENT MODEL DESCRIPTION

The FE model of a rigid pavement at JFK was created using the general-purpose FE software ABAQUS. The section was instrumented with pressure cells, strain gauges, and thermocouples (Garg et al., 2013). The pavement is composed of four layers: 500-mm-thick PCC slab, 100-mm-thick plant-mix macadam, 150-mm-thick dense-graded aggregate base (DGAB), and subgrade. The materials were assumed linear elastic, elastic modulus for the PCC, macadam, DGAB, and subgrade were 38,852; 2,000; 300; and 30 MPa, respectively. These values were provided by the FAA based on laboratory testing and typical values from other airfield pavement sections. The coefficient of thermal expansion for the PCC was 5.0×10^{-6} mm/mm/°F.

The three-dimensional FE model included special features regarding mesh, interaction between layers, and slab connectivity (see figure 7). The 7.6-m-long square PCC slab was meshed with four-node shell elements. The macadam and DGAB extended to infinity in the xz-plane; these layers were meshed with two types of elements: eight-node linear brick and infinite elements on

the boundaries. The subgrade extended to infinity along the three perpendicular directions. The interaction between layers was defined by a friction coefficient of 1.5 between the PCC and the macadam that allowed separation and a friction coefficient of 1.0 for the other interactions (Huang, 2004; Yoo et al., 2006). Finally, elastic rotational and translational springs connected the PCC slab to surrounding media. As discussed in section 3, the springs' magnitude controls the transfer of displacement and rotation among slabs. For instance, translational springs with very large magnitude represent full transfer of vertical displacement. If vertical displacement is not transferred from one slab to the other, the constant of the vertical spring is zero. Similar reasoning can be applied to rotational springs and a slab's bending.

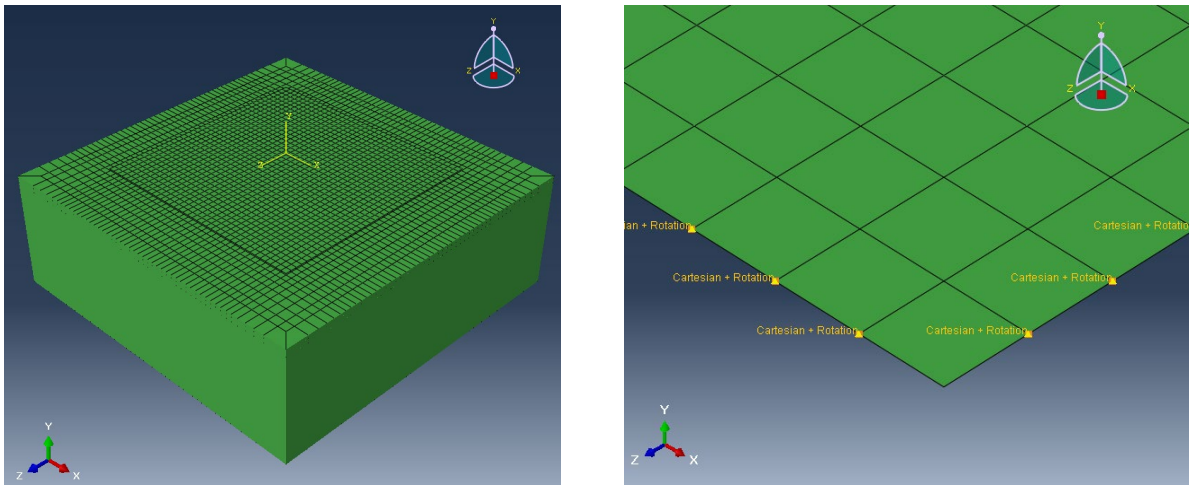

(a) (b)

Figure 7. Three-Dimensional FE Model in ABAQUS (a) With Detail of the Boundary Conditions (b)

4.2 MESH-SENSITIVITY ANALYSIS

Variation of longitudinal and transverse stresses through the slab's depth determined the optimal size of shell elements. Five mesh configurations with 9, 27, 81, 243, and 486 elements along the edge were considered; these are equivalent to 81; 729; 6,561; 59,049; and 236,196 finite elements in the slab. Arrays storing the stresses at 11 section points through the slab's center, edge, and corner were compared, using the finest mesh as benchmark. The analysis showed that elements smaller than 281 mm were appropriate, so a 200-mm element size was selected.

4.3 TEMPERATURE PROFILES

A modified version of the EICM, calibrated with experimental measurements, predicted temperature profiles within the concrete slab. EICM is a one-dimensional model that simulates heat and moisture flow within pavement structures; it is currently used by the Mechanistic-Empirical Pavement Design Guide (MEPDG) (ARA-ERES, 2014) to incorporate climate and environment. The main components of EICM are the climate–materials–structural model, frost-heave and settlement model, and infiltration-drainage model (Lytton et al., 1993). One of the most recent implementations of EICM is the software ILLI-THERM (Sen & Roesler, 2016). ILLI-THERM works on the same algorithms as EICM but excludes the infiltration-drainage model.

ILLI-THERM requires multiple user inputs (e.g., thermal conductivity, heat capacity, porosity) that need to be calibrated to produce realistic temperature profiles.

A Bayesian framework was adapted to perform the calibration in this study (Kennedy & O'Hagan, 2001). The framework optimized unknown material parameters to match ILLI-THERM's output and temperature measurements in the JFK section. After calibration, posterior distributions for each parameter provided insights about the significance of the input parameters. The adaptive Metropolis algorithm, an adaptive Monte Carlo Markov chain, was used to select samples to approximate the posterior distributions (Haario et al., 2001). In total, 309 samples were accepted from 5,000 simulations. The calibration improved the performance of ILLI-THERM by reducing the root mean square error (RMSE) by 15 %.

Calculated temperature profiles covered a wide range of average temperatures, temperature gradients, and temperature nonlinearity. The average temperature, the mean of temperatures across the slab's depth for every hour, varied between 35°F and 85°F. The temperature gradient, or difference between the temperature on the top and bottom of the slab, covered magnitudes between -20°F and 15°F. Finally, the nonlinear area parameter (NOLA) quantified the temperature profile's nonlinearity and varied between -3.81°F×mm and 1.9°F×mm (Hiller & Roesler, 2010).

4.4 MODEL VALIDATION

Comparison between measured and predicted strains at the bottom of the slab validated the FE model. Instrumented airfield rigid pavement at JFK provided measured strains (Garg et al., 2013); the measurements corresponded to the average of four readings during two testing periods, April and May 2011. The four readings were obtained from strain gauges located close to each corner of the slab: 1.5 m from the longitudinal joints and 0.25 m from the transverse ones. The predicted values resulted from the FE model subjected to the calculated hourly temperature profiles. Three conditions were simulated: In condition 1 (C1), the joints were free to displace and rotate; in condition 2 (C2), the joints were free to rotate, but displacements in the vertical direction were partially restrained; in condition 3 (C3), partial restriction as to vertical displacement and rotation along the joints was imposed.

Figure 8 compares the measurements and predictions for both testing periods. The responses used for validation were not highly sensitive to edge condition; however, as shown in sections 4.5 and 4.6, critical tensile stress and deflection were indeed affected by boundary condition. The RMSE varied between 10.3 and 14.4 microstrains, which corresponds to a variation of 3.8% and 5.2% from the average measurement, respectively. After validation, temperature profiles for seven additional testing periods were analyzed by the FE model. The seven testing periods are January, February, March, April, July, August, and December 2012. A total of 5,263 hours of temperature variations were modeled, and hourly critical tensile stress and deflection were analyzed.

4.5 CRITICAL TENSILE STRESSES

The critical tensile stress was defined as the highest tensile stress for all the sections' points of the shell elements in the concrete slab at a specific hour. Figure 8 shows the variation of the critical tensile stress for C2 and C3 with respect to C1 ($\sigma_{c,C1}$, $\sigma_{c,C2}$, and $\sigma_{c,C3}$, respectively). The solid line

represents cases where tensile stresses are equal to the critical stresses of C1; points above the equality line indicate conditions where the critical stress is higher than for the free condition.

As expected, assuming free boundaries along the joints did not result in a conservative analysis, as demonstrated by the cloud of points above the equality line. The free assumption provided the lowest tensile stresses among the three conditions; no stress ratio with respect to $C1$ was lower than 0.94, which happened in July 2012. The cloud of points also shows a value for the stress in C1 around 0.7 MPa, from which there was no significant difference between $\sigma_{c,C1}$ and $\sigma_{c,C2}$. For instance, in May 2011, the average stress ratio between $\sigma_{c,C2}$ and $\sigma_{c,C1}$ was 1.02 when the stress was higher than 0.7 MPa. When $\sigma_{c,C1}$ was lower than 0.7 MPa, the average ratio was 1.55. The other testing periods displayed similar behavior, where the average stress ratio when $\sigma_{c,C1}$ >0.7 MPa varied from 1.01 to 1.08, and for $\sigma_{c,C1}$ <0.7 MPa varied between 1.33 and 1.62. Consequently, for the studied pavement structure, the stresses calculated assuming free condition and partial restriction as to vertical displacement are equivalent if $\sigma_{c,C1}$ >0.7 MPa. The cloud of points in figure 9 also shows stresses enclosed between two lines, one being the equality line and the other one the equality line plus 0.35 MPa. In other words, adding 0.35 MPa to the critical stress, assuming free edges, results in a conservative estimation of critical tensile stresses for the studied pavement with partially restrained edges.

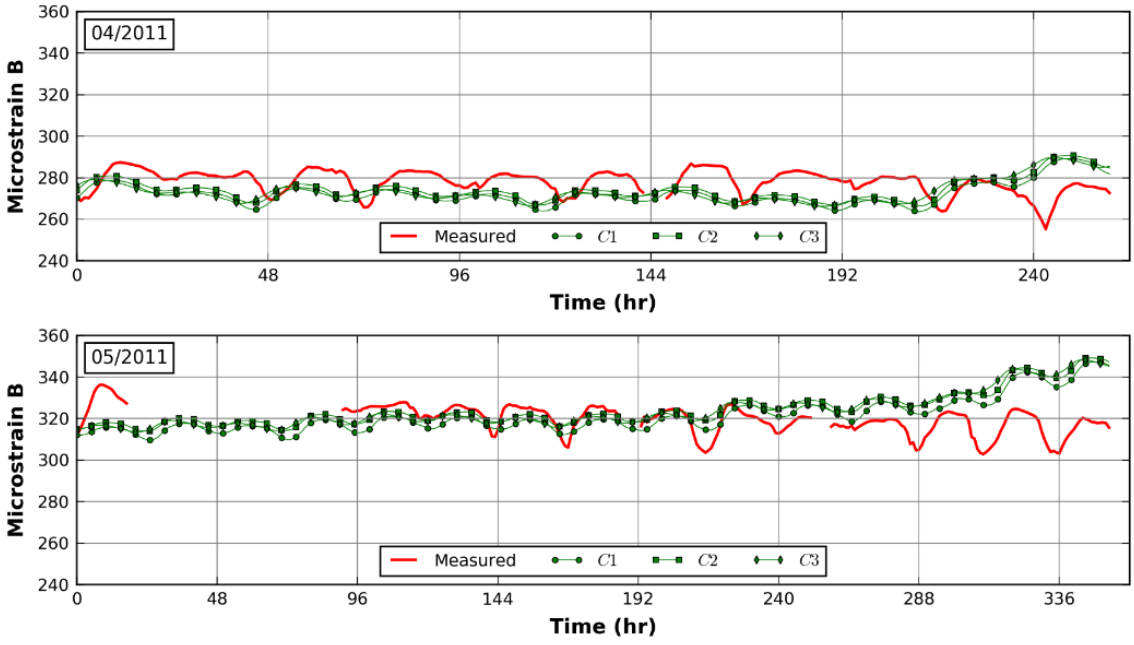

Figure 8. Comparison Between Measured and Calculated Corner Strain at the Bottom of the Slab

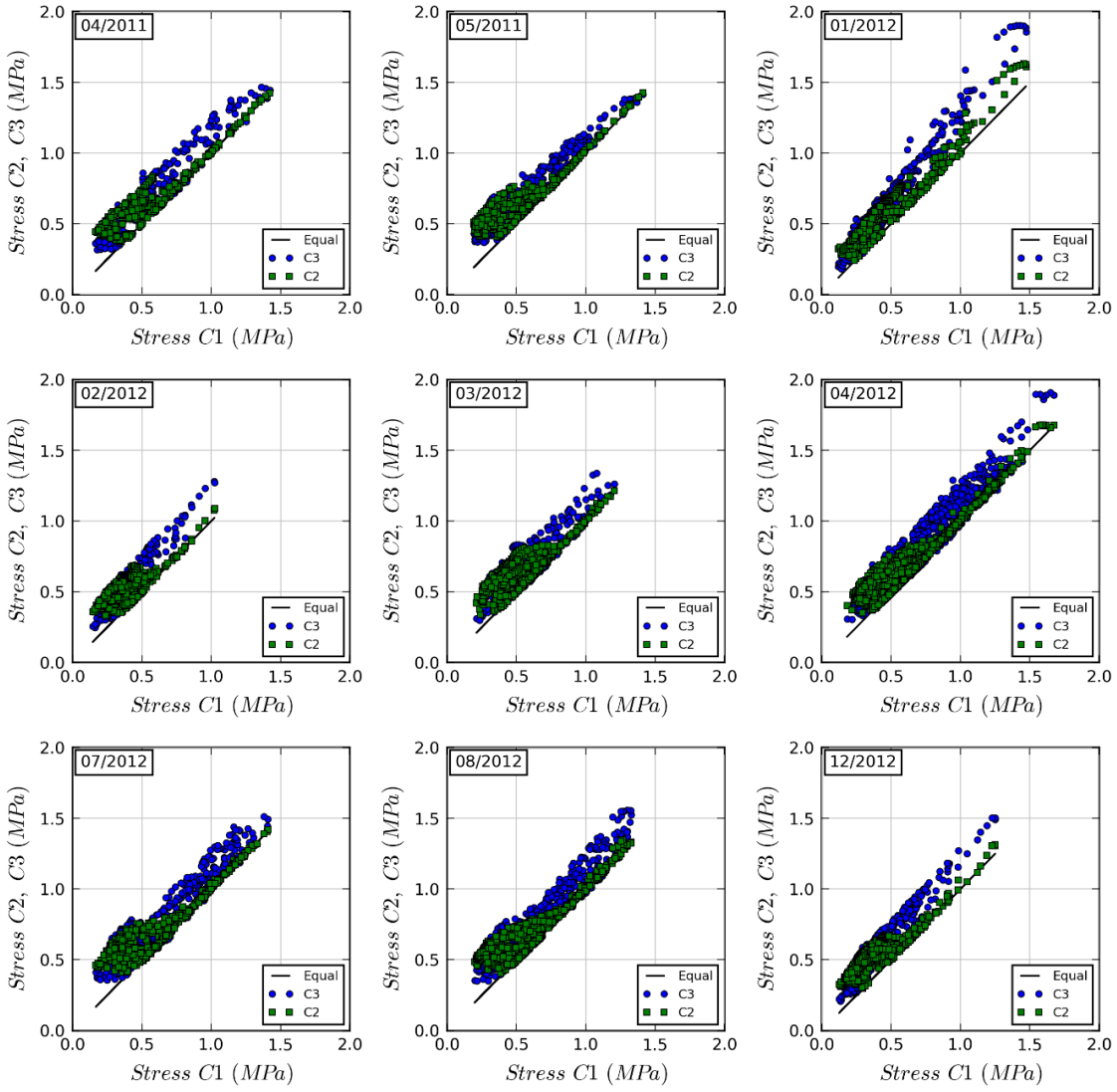

Figure 9. Variation of Critical Tensile Stresses for C2 and C3 With Respect to C1

The stress range was always higher for C3 than for C2. The largest range of stresses was observed for the testing period with the lowest temperatures: January 2012. During that period, the stress range for $\sigma_{c,C3}$ was 1.72 MPa, while that for $\sigma_{c,C2}$ was 1.39 MPa. This discrepancy is caused by the additional restraint to rotation in C3, which creates more stresses during temperature changes.

Figure 10 presents the distribution of the ratios of critical tensile stresses between $\sigma_{c,C3}$ and $\sigma_{c,C2}$. The only difference between the two conditions is the partial restriction to rotation in C3; the rotational restriction's relevance increases as the ratio departs from 1. The horizontal axis indicates ranges for the tensile-stress ratio, and the vertical axis is the percentage of events when the ratio falls in the corresponding range. For instance, in December 2012, the second bar indicates that the ratio of the critical stresses varied between 0.65 and 0.75 in 6.5% of the hours measured during December 2012. The restraint to rotation along the slab joints significantly affected the critical tensile stresses. First, the percentage of events with ratios between 0.95 and 1.05 (i.e., 5%

difference, or small impact) varied between 20.7% for December 2012 and 36.5% for March 2012. In contrast, the ratio was larger than 1.05 or lower than 0.95 in 70% of the cases for all the other testing periods.

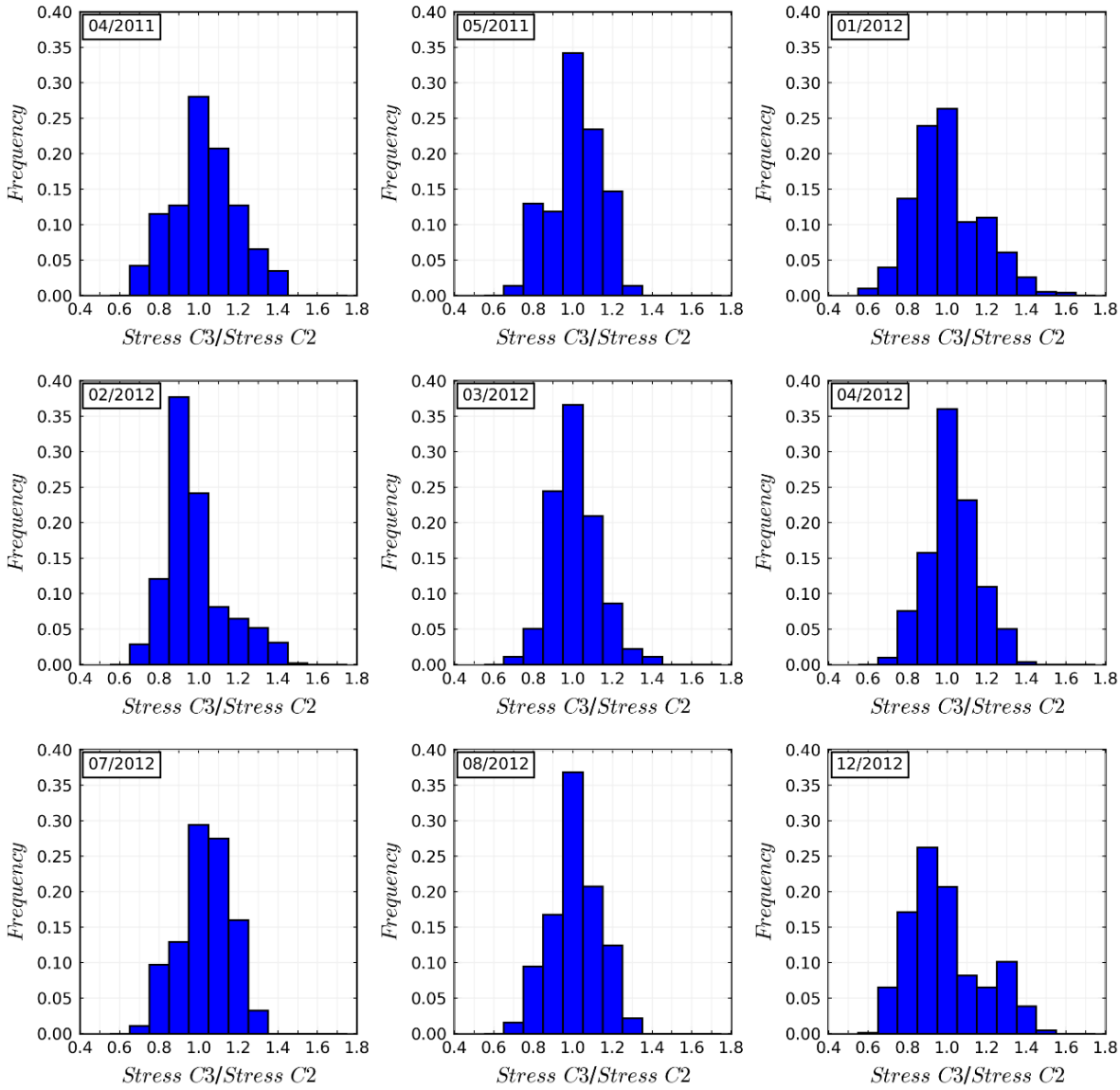

Figure 10. Distribution of Ratio Between Critical Tensile Stresses for C3 With Respect to C2

Temperature also influenced the impact of rotational restraint. The percentage of events when $\sigma_{c,C3}$ is lower than for $\sigma_{c,C2}$ is higher for colder temperatures. In January 2012, 42.6% of the events showed ratios lower than 0.95. Similarly, the percentage of events with ratios lower than 0.95 was 52.7% and 50.0% in February 2012 and December 2012, respectively. For the same two periods, $\sigma_{c,C3}/\sigma_{c,C2}$ was higher than 1.05 in 23.1% and 29.2% of the cases. For all the other testing periods, the situation was the opposite. The highest difference occurred in July 2012, when 46.6% of the events had ratios larger than 1.05 and 23.8% had ratios lower than 0.95.

December 2012 provided the highest percentage of cases with a difference of more than 25%: $\sigma_{c,C3}/\sigma_{c,C2}$ was higher than 1.25 in 23.8% and lower than 0.75 in 14.5% of the cases. However, having a large difference between critical stresses for C2 and C3 is not associated with low temperature. The other two periods with low temperatures, January 2012 and February 2012, did not have ratios above 1.25 and below 0.75 as significant as those of December 2012.

4.6 CRITICAL DEFLECTION

The critical deflection was defined as the difference between deformed coordinates at the corner and center of the slab with respect to the initial configuration of the corresponding testing period. Only values with positive curvature were analyzed because they contribute to faulting. The variation of the critical deflection for C2 and C3 with respect to C1 is presented in figure 11. The solid black line represents the critical deflection when there is no restriction as to vertical displacement and rotation (δ_{c1}) (i.e., equality line); green squares correspond to points when the slab edges are partially restrained as to vertical displacement (δ_{c2}); and blue circles are the critical deflection when both the vertical displacement and rotation are partially restrained (δ_{c3}).

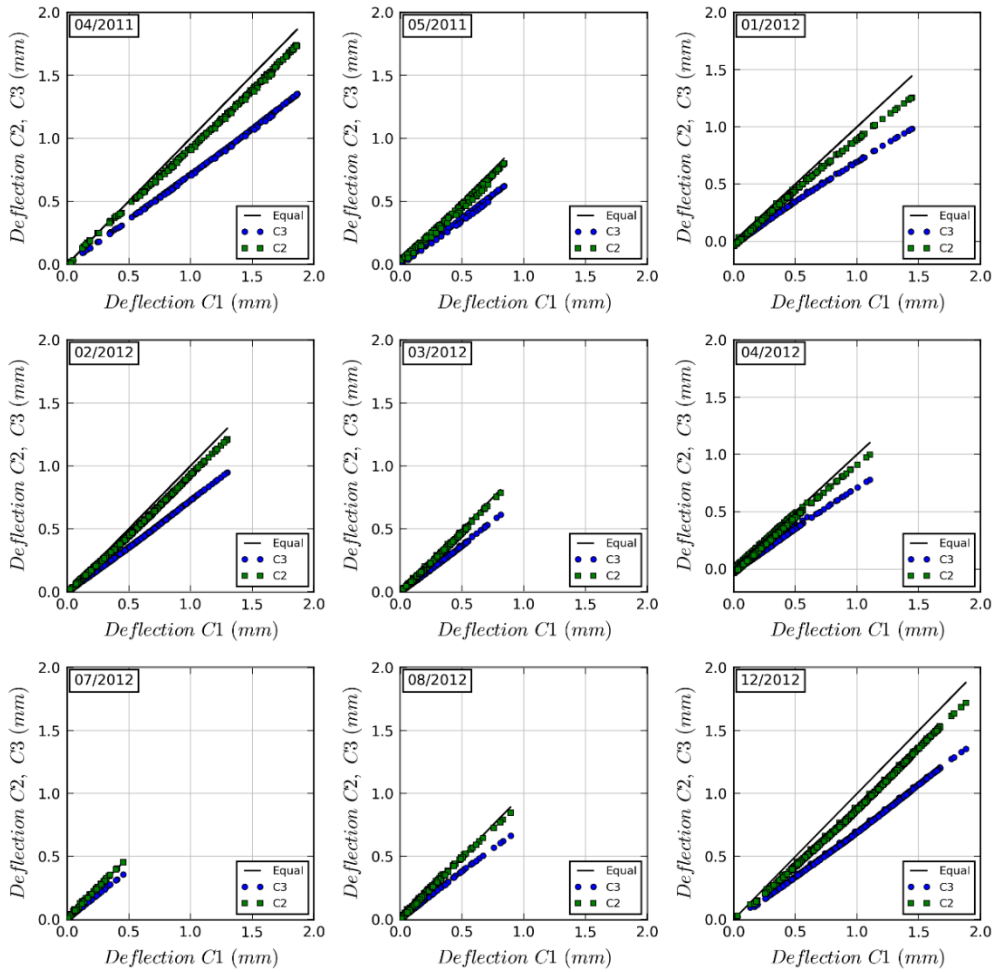

Figure 11. Variation of Critical Deflection for C2 and C3 With Respect to C1

The difference between C1 and C2 is smaller than the difference between C1 and C3, which indicates that rotational restriction's role in faulting is more relevant than restriction as to vertical displacement. The difference in slope of a linear regression of the cloud of points quantifies such relevance. The average slope for all testing periods for C2 and C3 were 0.944 and 0.738, respectively. In other words, restriction as to displacement causes 20% of the difference between the most restrained scenario and the free condition, while the other 80% is caused by the partial restriction as to rotation.

Even though it is expected that as the degree of restriction increases the vertical deflections decrease, summer months provided higher deflection for C2 with respect to C1. More specifically, for testing periods July 2012 and August 2012, δ_{c2} was higher than δ_{c1} in 94% and 62% of the cases, respectively. In contrast, instances when δ_{c3} was higher than δ_{c1} are rare. The highest percentage of events where the slab was partially restrained as to vertical deflection and rotation provided higher faulting deflections, 7.5% during the testing period July 2012.

4.7 SUMMARY

The validated FE model of an airfield rigid pavement showed the relevance of slab joints' rotation on critical curling stresses and deflections. The validation used strain measurements from JFK during April and May 2011. The model included 5,263 hours of temperature profiles determined using thermocouple readings and the EICM.

Three joint conditions quantified the impact of the restriction as to rotation. The results revealed that joint rotation affects the critical curling stresses and deflections. In the case of critical curling stresses, partially restraining joint rotation resulted in significant difference in 70% of the cases. For critical deflection, 80% of the difference between the free condition and the most restrained case is caused by the partial rotational restraint, while 20% is caused by the partial restriction as to vertical displacement. Finally, calculations assuming free joints can provide initial estimation of critical curling responses for other joint conditions. In summary, joint rotation significantly affects both critical stresses and deflections; and it should be included in the long-term performance analysis of airfield rigid pavement.

5. BLOWUP ANALYSIS

Analytical expression for static stability of a rectangular slab with two simply supported and two elastically restrained edges is presented in this section. The linear elastic isotropic slab, which can represent a rigid pavement, rested on an elastic foundation and was loaded by a uniform in-plane axial load per unit length along the edges. The partially restrained edges are connected to the ground by translational and rotational elastic springs; an appropriate magnitude of the springs can capture classical boundary conditions such as free, simply supported, and clamped edges. Results from classical boundary conditions and an FE model were used to validate the proposed stability equation. The generalized boundary conditions were found to change the critical load by a factor of two and greatly affected the first buckling-mode shape of a typical concrete pavement. The critical load was not sensitive to the slab's geometry if the length was four times longer than the width, but this is not the case for small aspect ratios. Finally, the translational spring was found to be a defining factor in determining the influence of the other variables on the critical load.

5.1 STRUCTURAL MODEL AND STABILITY EQUATION

Consider a slab of length L and width $2bL$ (aspect ratio = $2b$) made of a linear elastic material with elastic modulus E and Poisson's ratio ν. The slab, whose thickness h is small compared to the shortest plan dimension, is supported on an elastic foundation with modulus of subgrade reaction Λ. The origin of the coordinate system is located at the midpoint of the left-hand-side edge of the slab, with the x'- and y'-axes pointing along the length and width of the slab, respectively, as shown in figure 12.

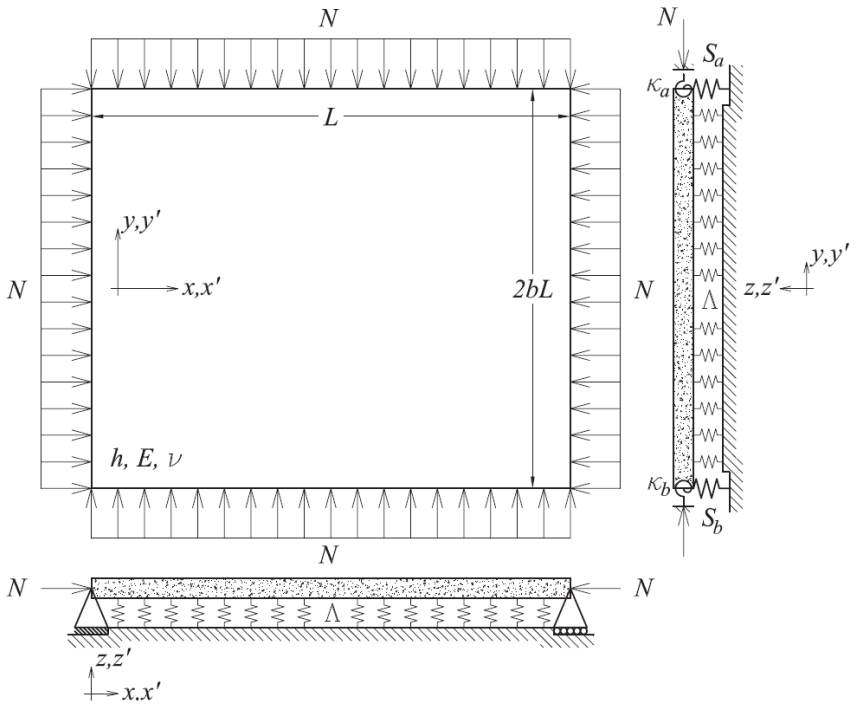

Figure 12. Rectangular Slab With Two Simply Supported Edges and Two Elastically Restrained Edges

The slab is loaded along the x' and y' directions by in-plane load per unit length N. The slab was assumed to be simply supported along edges parallel to the y' axis. Along the edges parallel to the x' axis, generalized boundary conditions were assumed; the vertical displacement and the rotation were partially restrained by translational and rotational springs of magnitude S_a , S_b, κ_a, and κ_b, respectively, as shown in figure 12. Traditional boundary conditions can be captured by assigning appropriate values to the spring constants. As shown in previous sections, if S_a and S_b are significantly large, the edge of the slab would not have any vertical displacement. If κ_a =κ_b=0, the slab would be free to rotate, which constitutes a simply supported condition. In contrast, if both rotational springs approach the infinite, the edge cannot rotate and a clamped boundary condition is obtained.

Based on thin-slabs theory, the partial differential equation for the vertical deflection w of a slab resting on an elastic foundation is given by

$$D\left[\frac{\partial^4 w}{\partial x'^4} + \frac{\partial^4 w}{\partial x'^2 \partial y'^2} + \frac{\partial^4 w}{\partial y'^4}\right] + N\left[\frac{\partial^2 w}{\partial x'^2} + \frac{\partial^2 w}{\partial y'^2}\right] + \Lambda w = 0 \quad (21)$$

where $D = Eh^3/12/(1-\nu^2)$ is the slab's bending stiffness. Along the elastically restrained edges, the shear force and bending moment are

$$V(x', bL) = S_a w(x', bL) \quad (22)$$
$$V(x', -bL) = -S\_b\, w(x', -bL) \quad (23)$$
$$M(x', bL) = \kappa_a \theta(x', bL) \quad (24)$$
$$M(x', -bL) = -\kappa_b \theta(x', -bL) \quad (25)$$

where V, M, and θ are the shear force, bending moment, and rotation of the slab. Normalizing lengths with respect to L, the partial differential equation for w becomes

$$\frac{\partial^4 w}{\partial x^4} + \frac{\partial^4 w}{\partial x^2 \partial y^2} + \frac{\partial^4 w}{\partial y^4} + k\left[\frac{\partial^2 w}{\partial x^2} + \frac{\partial^2 w}{\partial y^2}\right] + \lambda^4 w = 0 \quad (26)$$

where the dimensionless buckling-load coefficient, k, and dimensionless subgrade-stiffness coefficient, λ, are

$$k = \frac{NL^2}{D} \quad (27)$$
$$\lambda^4 = \frac{\Lambda L^4}{D} \quad (28)$$

Because edges parallel to the y' axis are simply supported, the solution of equation 26 can be assumed as follows:

$$w(x, y) = f(y) \sin \alpha x \quad (29)$$

where $\alpha = n\pi$, with n being an integer. Substituting equation 29 into equations 26 and 22-25, the differential equation for $f(y)$ is

$$\frac{d^4 f}{dy^4} + (k - 2\alpha^2)\frac{d^2 f}{dy^2} + (\alpha^4 - k\alpha^2 + \lambda^4) f = 0 \quad (30)$$

and its boundary conditions are

$$f'''(b) - [\alpha^2(2-\nu) - k] f'(b) = T_a f(b) \quad (31)$$
$$f'''(-b) - [\alpha^2(2-\nu) - k] f'(-b) = -T_b f(-b) \quad (32)$$
$$f''(b) - \nu\alpha^2 f(b) = -R_a f'(b) \quad (33)$$
$$f''(-b) - \nu\alpha^2 f(-b) = R_b f'(-b) \quad (34)$$

where $T_a = S_a L^3/D$, $T_b = S_b L^3/D$, $R_a = \kappa_a L/D$, and $R_b = \kappa_b L/D$ are the translational and rotational stiffness indexes along both edges of the slab, respectively. Equation 30 is a fourth-order linear differential equation with constant coefficients, with the characteristic equation:

$$\beta^4 + (k - 2\alpha^2)\beta^2 + (\alpha^4 - k\alpha^2 + \lambda^4) = 0 \tag{35}$$

then:

$$\beta^2 = \frac{1}{2}\left[-(k - 2\alpha^2) \pm \sqrt{k^2 - 4\lambda^4}\right] \tag{36}$$

The solution $f(y)$ depends on the nature of the roots β, and three cases are identified:

- Case 1: if $\Delta > 0$ and $2\alpha^2 - k > \sqrt{\Delta}$, then the roots are real, and the solution is

$$f(y) = c_1 e^{\beta_1 y} + c_2 e^{-\beta_1 y} + c_3 e^{\beta_2 y} + c_4 e^{-\beta_2 y} \tag{37}$$

with

$$\beta_1^2 = \frac{2\alpha^2 - k + \sqrt{\Delta}}{2} \tag{38}$$

$$\beta_2^2 = \frac{2\alpha^2 - k - \sqrt{\Delta}}{2} \tag{39}$$

- Case 2: If $\Delta > 0$ and $2\alpha^2 - k < \sqrt{\Delta}$, then the roots are complex, and the solution is

$$f(y) = c_1 e^{\beta_1 y} + c_2 e^{\beta_2 y} + c_3 \sin \beta_2 y + c_4 \cos \beta_2 y \tag{40}$$

with

$$\beta_1^2 = \frac{2\alpha^2 - k + \sqrt{\Delta}}{2} \tag{41}$$

$$\beta_2^2 = -\frac{2\alpha^2 - k - \sqrt{\Delta}}{2} \tag{42}$$

- Case 3: if $\Delta < 0$, then the roots are complex conjugate, and the solution is

$$f(y) = c_1 e^{sy} \cos ty + c_2 e^{sy} \sin ty + c_3 e^{-sy} \cos ty + c_4 e^{-sy} \sin ty \tag{43}$$

with

$$\beta_1^2 = \frac{2\alpha^2 - k + \sqrt{4\lambda^4 - k^2}\,i}{2} = s + ti \tag{44}$$

$$\beta_2^2 = \frac{2\alpha^2 - k - \sqrt{4\lambda^4 - k^2}i}{2} = -s + ti \tag{45}$$

Substituting $f(y)$ from equations 37, 40, and 43, into the boundary conditions in equations 31-34, a homogenous system of equations of the form $[A]_{4\times4} \cdot [C]_{4\times1} = [0]_{4\times1}$ can be built, where $[A]_{4\times4}$ stores the coefficient of c_1, c_2, c_3, and c_4, which are grouped in $[C]_{4\times1}$. The critical axial load N_{critc} is the value of N that makes the determinant of $[A]$ equal to zero. Equating the determinant $[A]$ to zero results in the characteristic stability equation, which, regardless the form of $f(y)$, can be written as follows:

$$[RT]_{1\times16}[COEF]_{16\times t}[TRIG]_{t\times1} + [RT]_{1\times16}[REM]_{16\times1} = 0 \tag{46}$$

where: t: integer whose value depends on the type of roots: t=4 for real roots (Case 1), t=8 for complex roots (Case 2), and t=11 for complex conjugate roots (Case 3); $[RT]_{1\times16}$: vector containing combinations of R_a, R_b, T_a, and T_b; $[TRIG]_{t\times1}$: vector of trigonometric functions; $[COEF]_{16\times t}$: = matrix storing coefficients of trigonometric functions in $[TRIG]_{t\times1}$; and $[REM]_{16\times1}$: terms not multiplying trigonometric functions.

The values of $[RT]$, $[TRIG]$, $[COEF]$, and $[REM]$ for the three types of solution are provided in appendix B. $[RT]$ is the same for all the cases and corresponds to the first column in the tables; $[TRIG]$ depends on the solution for $f(y)$, and it is given by the heading of the tables in the mentioned appendix; $[COEF]$ are the entries in the tables; and $[REM]$, which is different than zero only when the roots are real, is given in the last table of the appendix. The buckling-mode shapes are obtained by replacing the critical load in the homogeneous system $[A] \cdot [C] = [0]$, solving for one of the four constants in $[C]$, and substituting into the corresponding $f(y)$ (equations 37, 40, or 43).

An FE model was developed using ABAQUS to verify the results of the proposed equations. Four-node, full-integration shell elements were used to model the slab resting on an elastic foundation. Two-node, three-dimensional connector elements with translational and rotational spring constant simulated the semirigid connections. A biaxial uniform load per unit length was applied along the edges of the slab, and an eigenvalue buckling analysis was performed. The vertical displacements of the simply supported edges, the ones parallel to the y' axis, were fully restrained as to vertical displacement. In addition, a kinematic constraint was created to guarantee that the two opposite edges have negligible displacement in the y' direction. The resulting critical loads were compared with results obtained by using the stability equation in equation 46.

5.2 SLAB WITH CLASSICAL BOUNDARY CONDITIONS

Consider a slab with simply supported edges parallel to the y' axis, and the other two edges fully restrained as to vertical displacement (i.e., S_a=S_b tending to infinity). When $\Delta > 0$ and $2\alpha^2 - k > \sqrt{\Delta}$, the terms in equation 46 are obtained by finding the limit when $S_a = S_b \to \infty$. From table B-7 and substituting into equation 46:

$$[RT]_{1\times4}[COEF\,]_{4\times4}[\,TRIG]_{4\times1} + \,[RT]_{1\times4}[REM]_{4\times1} = 0 \tag{47}$$

$$\begin{pmatrix} R_aR_b \\ R_a \\ R_b \\ 1 \end{pmatrix}^T \begin{pmatrix} -2B_p^2 & 2B_m^2 & 0 & 0 \\ 0 & 0 & -2B_mB_p^2 & 2B_m^2\,B_p \\ 0 & 0 & -2B_mB_p^2 & 2B_m^2B_p \\ -2B_m^2B_p^2 & 2B_m^2B_p^2 & 0 & 0 \end{pmatrix} \begin{pmatrix} \cosh(2b\beta_1 - 2\,b\,\beta_2) \\ \cosh(2b\beta_1 + 2b\beta_2) \\ \sinh(2b\beta_1 - 2b\beta_2) \\ \sinh(2b\beta_1 + 2b\beta_2) \end{pmatrix} + \begin{pmatrix} R_aR_b \\ R_a \\ R_b \\ 1 \end{pmatrix} \begin{pmatrix} 8\beta_1\beta_2 \\ 0 \\ 0 \\ 0 \end{pmatrix} = 0 \tag{48}$$

where $B_p = \beta_1 + \beta_2$ and $B_m = \beta_1 - \beta_2$. After performing the matrix operations, equation 48 becomes

$$\begin{aligned} -2B_m^2B_p^2\cosh(2b\beta_1 - 2b\beta_2) \; &+ 2B_m^2B_p^2\cosh(2b\beta_1 + 2b\beta_2) \\ &+ R_a\big[2\,B_m^2B_p\sinh(2b\beta_1 + 2b\beta_2) \\ &- 2B_mB_p^2\sinh(2b\beta_1 - 2b\beta_2)\,\big] \\ &+ R_b\big[2\,B_m^2B_p\sinh(2b\beta_1 + 2b\beta_2) \\ &- 2\,B_mB_p^2\sinh(2b\beta_1 - 2b\beta_2)\,\big] \\ &+ R_aR_b\big[2B_m^2\cosh(2b\beta_1 + 2b\beta_2) \\ &- 2B_p^2\cosh(2b\beta_1 - 2b\beta_2) \; + 8\beta_1\beta_2\big] = 0 \end{aligned} \tag{49}$$

If the slab is simply supported along all edges, the stability equation when the roots are real is obtained making $R_a = R_b = 0$. Then equation 49 becomes

$$(\beta_1^2 - \beta_2^2)^2\sinh(2b\beta_1)\sinh(2b\beta_2) = 0 \tag{50}$$

In addition, $R_a = R_b \to \infty$ provides the equations for a clamped slab. Similar procedures can be followed for the other cases (i.e., complex and complex conjugate roots). Tables 1 and 2 summarize the stability equations for a slab with two edges simply supported and clamped, respectively.

Table 1. Stability Equations for a Slab With All Edges Simply Supported

Case	Stability Equation
$\Delta > 0,\ 2\alpha^2 - k > \sqrt{\Delta}$	$(\beta_1^2\ - \beta_2^2)^2\sinh(2b\beta_1)\sinh(2b\beta_2)\ = 0$
$\Delta > 0,\ 2\alpha^2 - k < \sqrt{\Delta}$	$4\,(\beta_1^2 + \beta_2^2)^2\sin(b\beta_2)\cos(b\beta_2)\sinh(2b\beta_1) = 0$
$\Delta < 0$	$8s^2t^2[\cos(4bt) - \cosh(4bs)\,] = 0$

Table 2. Stability Equations for a Slab With Two Edges Simply Supported and Two Edges Clamped

Case	Stability Equation
$\Delta > 0,\ 2\alpha^2 - k > \sqrt{\Delta}$	$2(\beta_1 + \beta_2)^2 \cosh[2\ b\ (\beta_1 - \beta_2)] - 2\ (\beta_1 - \beta_2)^2 \cosh[2\ b\ (\beta_1 + \beta_2)] = 0$
$\Delta > 0,\ 2\alpha^2 - k < \sqrt{\Delta}$	$4\ \beta_1\beta_2 \cos^2(b\beta_2) \cosh(2b\beta_1) - 4\beta_1\beta_2(b\ \beta_2) \cosh(2b\beta_1) - 4(\beta_1^2 - \beta_2^2) \sin(b\beta_2) \cos(b\beta_2) \sinh(2b\beta_1) = 0$
$\Delta < 0$	$s^2 \cos(4bt) - t^2 \cosh(4bs) = 0$

Table 3 compares the critical load calculated using the proposed equations, the FE model, and the values reported by Yu and Wang (2008) for two boundary conditions: simply supported and clamped. The slab's length is twice its width (b=0.25), and three support conditions were assumed (λ=0, 2, and 5). The table also shows the percentage difference with respect to the proposed method. As shown, the agreement is excellent.

Table 3. Comparison Among Yu and Wang (2008), Equations, and ABAQUS for b=0.25

Boundary Condition	λ	Proposed Method	Yu and Wang (2008)		ABAQUS	
		k	k	Difference (%)	k	Difference (%)
Simply Supported	0	49.3475	49.35	-0.005	49.2219	0.255
	2	49.6722	49.67	0.004	49.5546	0.237
	5	62.0136	62.02	-0.010	62.2191	-0.331
Clamped	0	150.9549	150.99	-0.023	149.7369	0.807
	2	151.2148	151.24	-0.017	150.0006	0.803
	5	158.1408	158.13	0.007	159.9969	-1.174

5.3 CRITICAL LOAD OF CONCRETE PAVEMENT

Consider a square slab (L=$2bL$=4.0 m) of a rigid pavement whose longitudinal joints are assumed simply supported. The slab has a thickness of h=0.3 m, and it is resting on an elastic foundation with modulus of subgrade reaction of Λ=18.2 MN/m^3. The concrete has an elastic modulus of E=25000 MPa and a Poisson's ration of ν=0.15. The transverse joint ahead of traffic is in good condition, meaning there is a good transfer of shear force and bending moment to the next slab (κ_a=1.439×10^6 kN×m/rad/m and T_a=8.991×10^5 N/m/m). Conversely, the other transverse joint is progressively deteriorating to the point there is no load transfer to the adjacent slab. The objective is to find the effect of joint deterioration on the critical load and the first mode of buckling.

The bending stiffness of the slab is $D = Eh^3/12/(1-\nu^2)$=57.5 MN×m. The translational and rotational stiffness indexes of the joints ahead of traffic are T_a=S_aL^3/D=100 and R_a=κ_aL/D=1,000. The parameter associated with the elastic foundation is λ=$\Lambda L^4/D$=3.0. Six joint-deterioration conditions were considered by assigning different values to the parameters T_b and R_b. The values ranged between R_a=0.001 and S_a=0.01, which represents no load transfer between slabs, to R_a=200 and S_a=2,000.

The blowup loads N_{critc} for the various joint conditions were calculated using equation 46 and are summarized in table 4. As the stiffness of the joint is reduced, the slab's restriction to motion also decreases. This reduction in stiffness, as expected, decreased the magnitude of the critical load. Also, for the selected values of R_a and S_a, the change of N_{critc} is almost linear, highlighting the relevance of accurate characterization of joint deterioration for prediction of the critical load of concrete pavement.

Table 4. Effect of Joint Deterioration on Critical Load

Joint Condition	k	N_{critc} (kN/m)
R_a=0.001, $S_a = 0.01$	18.10	65,110.22
R_a=10, $S_a = 1$	21.51	77,377.14
R_a=20, $S_a = 10$	24.36	87,605.53
R_a=50, $S_a = 100$	29.16	104,861.5
R_a=100, $S_a = 1000$	34.24	123,156.9
R_a=200, $S_a = 2000$	37.79	135,912.0

Figure 13 shows the effect of joint deterioration on normalized buckling-mode shapes. If the joint is in good condition (S_b=2000 and T_b=200), the maximum deflection is located towards the center of the slab. As the transverse joint deteriorates, the point of maximum deflection shifts toward the weaker joint. For the weakest joint condition, not only is the maximum deflection located at the joint but also the curvature of the slab has changed. The deformed shaped agrees with the deformation of concrete pavement when it fails by buckling.

It should be highlighted that the proposed method has the capability of considering rotational and translational spring stiffness independent from each other. However, in the case of actual concrete pavements, joint deterioration causes stiffness reduction in a coupled fashion, indicating that a function relating R_a to S_a and R_b to S_b must be included. Consequently, some of the $R_b - S_b$ combinations in figure 13 are not likely to occur in real life. This observation also applies to the results in sections 5.4–5.7.

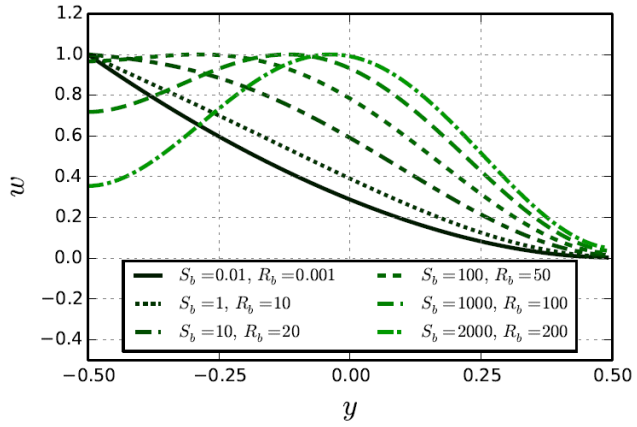

Figure 13. Effect of Joint Deterioration on Mode Shapes

5.4 EFFECT OF JOINT STIFFNESS ON CONCRETE-PAVEMENT BLOWUP

The influence of the degree of constraint as to vertical displacement and rotation on the critical load of a square slab was studied. Two support cases were considered: For the first, no elastic foundation was considered ($\lambda = 0$); and for the second , the slab geometry, material properties, and modulus of subgrade reaction provided λ=2. Slab edges not being simply supported were assumed to have the same degree of constraint (R_a=R_b and S_a=S_b); R_a ranged between 10^{-3} and 10^4, while S_a varied between 10^{-2} and 10^4. The range of values for R_a and S_a can be physically interpreted as various joint-deterioration degrees.

Figures 14 and 15 show the variation of the dimensionless buckling-load coefficient k with S_a and R_a for both values of λ. If the vertical restraint was low (S_a<20), the rotational restraint had negligible effect on the critical load. For instance, when λ=2, k increased only 0.02% after increasing R_a from 10^{-3} to 10^4, indicating that vertical displacement of the edges is more important than rotation. In contrast, the relevance of R_a is very high as the magnitude of S_a is higher, with k almost doubled when changing the magnitude of the rotational stiffness index between its extreme values when S_a=10^4 (increment of 91% and 87% for λ=0 and 2, respectively).

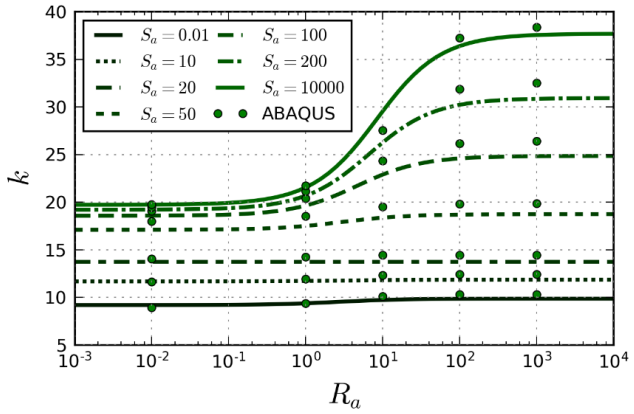

Figure 14. Effect of Semirigid Connections of Critical Load for λ=0

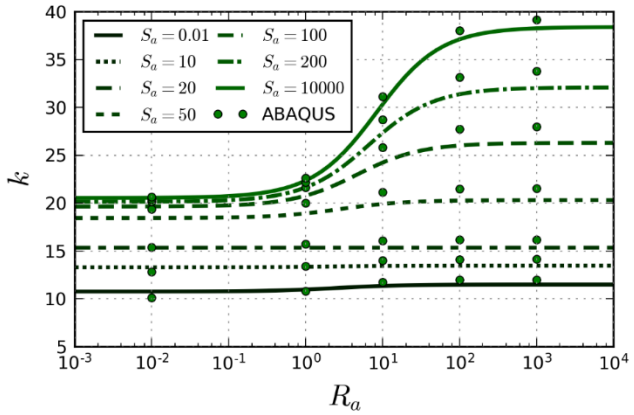

Figure 15. Effect of Semirigid Connections of Critical Load for $\boldsymbol{\lambda}$=2

Similarly, the highest influence of the translational restraint was seen for the highest magnitude of R_a. If R_a=10^{-3}, the increment of k when there is no elastic foundation and S_a changes from 50 to 10^4 is 15%. In contrast, for the same change in S_a but for R_a=10^4, the dimensionless buckling-load coefficient doubled from k=18.73 to 37.67. In general, three zones can be identified to characterize the effect of R_a and S_a on the critical load. If R_a<0.1 and R_a>100, the rotational stiffness index has no effect on the critical load, regardless the magnitude of S_a. Conversely, if 10< R_a<100, the change of k with R_a is almost linear in the semilogarithmic scale. These results indicate that preventive measures against concrete-pavement blowup should include joint-quality inspection.

Figure 16 compares the results from the proposed equation and ABAQUS. The continuous line represents the values predicted by the FE model. The figure also shows the equation of a linear fit to the cloud of points, which identifies a good agreement between the results obtained using equation 46 and ABAQUS. However, it is worth noting that the proposed solution does not need any special-purpose software like ABAQUS and can be easily implemented.

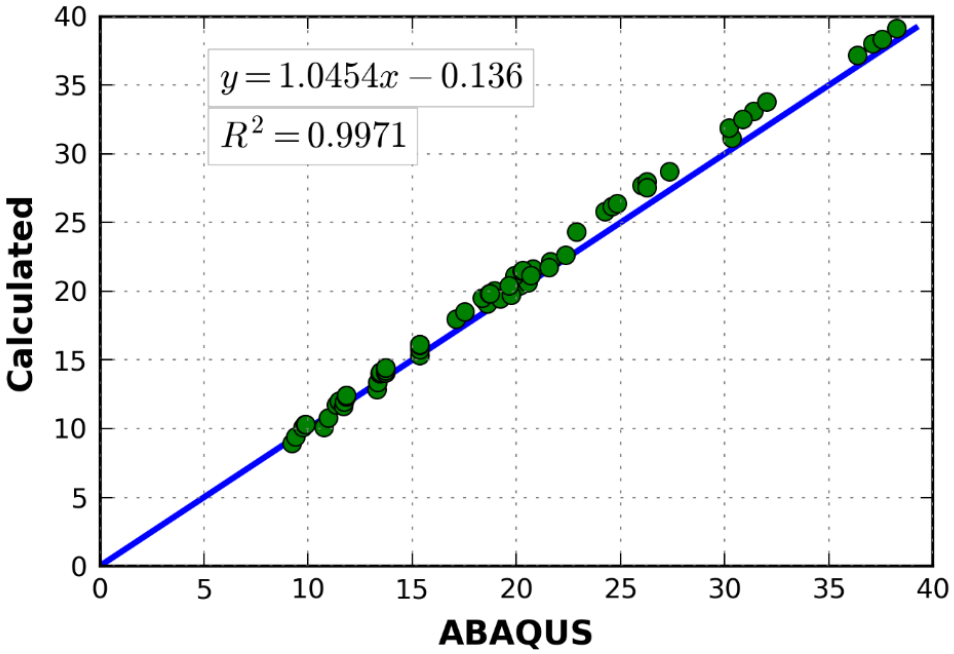

Figure 16. Comparison Between Calculated Values and ABAQUS

5.5 EFFECT OF SLAB SIZE ON CONCRETE-PAVEMENT BLOWUP

The effect of a slab's aspect ratio on the critical load under various restraint conditions was analyzed. Figure 17 shows such variation when b changed between 0.3 and 2.0; b=0.3 represents a slab whose width is 60% longer than its length. Variation of half the aspect ratio can be physically interpreted as a slab with a fixed length whose width continuously decreases. Values of aspect ratio that are too small or too big can represent structural behavior other than that of a slab, which is out of the scope of this work. The results presented were obtained assuming S_a=S_b and R_a=R_b.

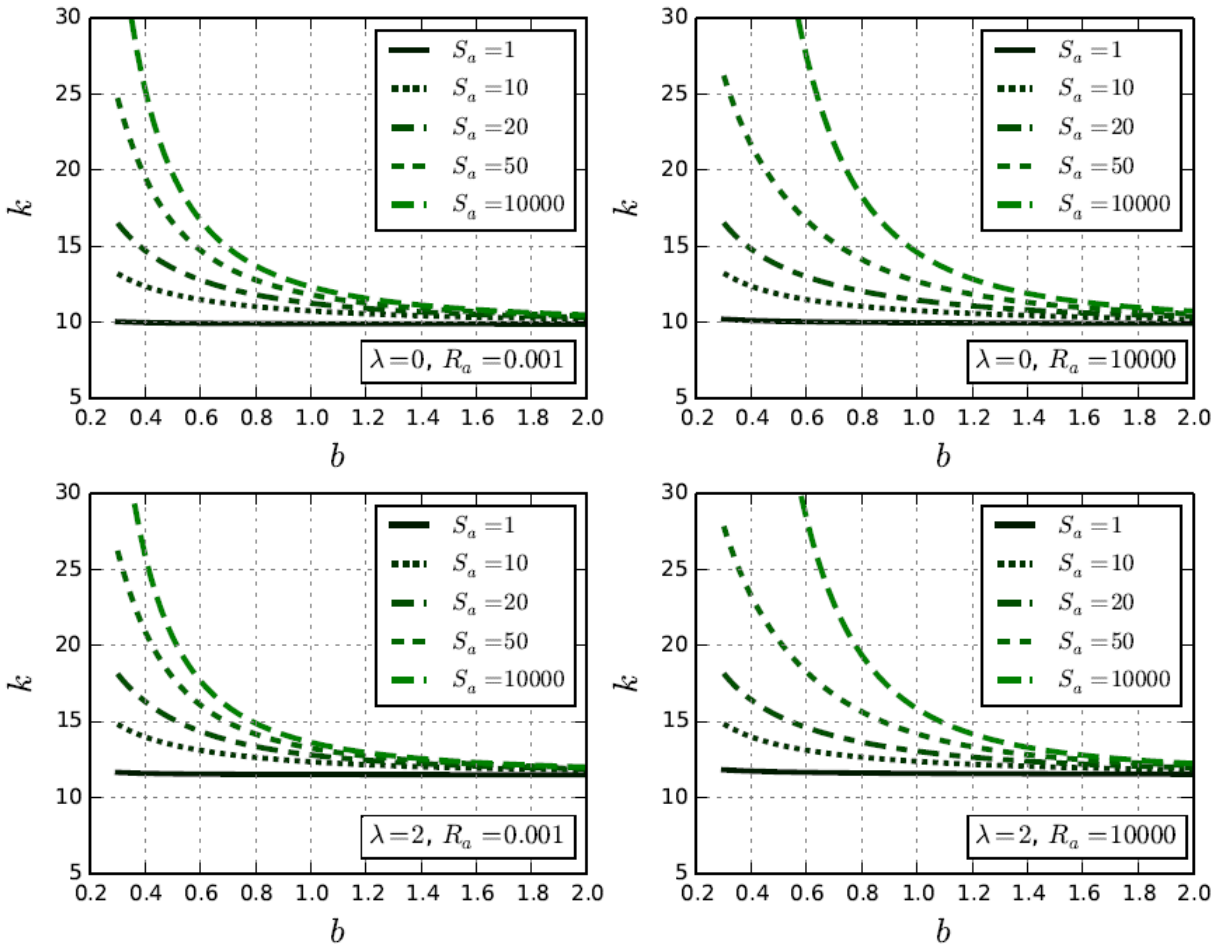

Figure 17. Effect of Size on Critical Load

The dimensionless buckling-load coefficient k is insensitive to aspect ratio if S_a is low, regardless of the rotational restraint for both values of λ considered. For instance, if R_a=10^4, S_a=1, and λ=2, k changes 2.6% between the two extreme values of b. As vertical restraint increased, critical load augmented and the aspect ratio's influence was significant. For the same case (λ=2 and R_a=10^4) and S_a=50, the critical load decreased 42% when b changed from 0.3 to 2.0. Similarly, the impact of R_a on the critical load became greater as S_a increased. These results show that proper characterization of vertical displacement at the edges of the slab is crucial for accurate calculation of the critical load.

Most of the influence of the semirigid connections happened for b less than 1.2. As b increased beyond 1.2, the influence of the rotational and translational stiffness indexes decreased to the point that all lines became almost coincidental and parallel to each other. In other words, the boundary conditions of the edges that are not simply supported become irrelevant once the bending of the slab is predominantly in one direction, that is, when the slab's width is significantly greater than its length.

In summary, a slab's aspect ratio is a relevant factor when determining critical load; and its influence is coupled with the boundary conditions. Consequently, care should be exercised when using solutions that consider slabs with infinite in-plane dimensions. In addition, in the design of concrete pavement, a slab's aspect ratio should be kept small to minimize the likelihood of blowup.

5.6 PRACTICAL IMPLEMENTATION

Rigid-pavement design methodologies, such as the MEPDG, account for joint deterioration using empirical equations (ARA-ERES, 2004). In the MEPDG, joint deterioration is related to load-transfer efficiency, LTE, which is defined as the ratio between the approach-slab deflection, w_a, and the leave-slab deflection, w_l, in percentage (see figure 18). In other words:

$$LTE = \frac{w_a}{w_l} \times 100 \tag{51}$$

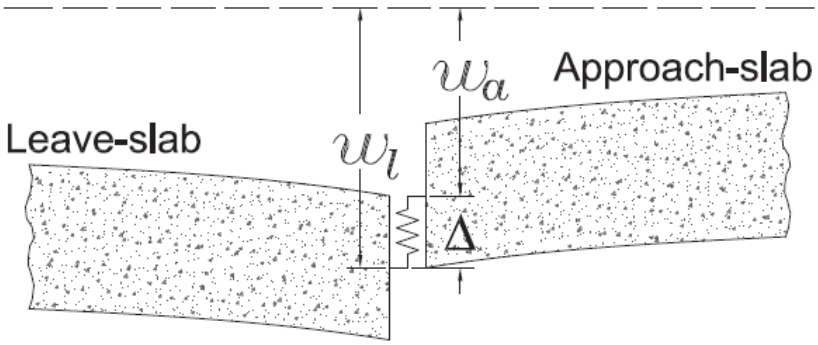

Figure 18. Load-Transfer Efficiency and Translational Spring Constant

The LTE is affected by aggregate interlock, quality of the support of the concrete slab, and details of the dowel system connecting the two slabs, and can be calculated as follows (ARA–ERES 2004):

$$LTE = 100\left[1 - \left(1 - \frac{LTE_{dowel}}{100}\right)\left(1 - \frac{LTE_{agg}}{100}\right)\left(1 - \frac{LTE_{base}}{100}\right)\right] \tag{52}$$

where LTE_{dowel}, LTE_{agg}, and LTE_{base} are the contributions to LTE of dowel systems, aggregate interlock, and supporting base, respectively.

The spring connecting the two slabs in the vertical direction develops a force V_s equal to

$$V_s = k_s \times \Delta = k_s \times (w_l - w_a) = k_s \times \left(1 - \frac{LTE}{100}\right) w_l \tag{53}$$

where k_s is the spring stiffness, and Δ is the spring deformation. The shear equilibrium at the joint between the approach- and leave-slabs requires

$$V_l - V_a \;=\; V_s = k_s \times \left(1 \;- \frac{LTE}{100}\right) w_l \tag{54}$$

where V_l and V_a are the shear at the edges of the leave- and approach-slabs. In equation 54, V_l, V_a, and w_l can be calculated by setting the equilibrium equations for each slab and using the appropriate boundary conditions. Joint deterioration can be accounted for through changes in LTE as implemented in MEPDG. It should be highlighted that MEPDG does not take into account transfer of rotation, but similar continuity conditions as in equation 54 can be established for rotation at slab joints.

5.7 SUMMARY

A stability equation was derived for a linear elastic slab resting on an elastic foundation with two simply supported and two partially restrained edges. The stability equation enables the critical-load calculation using a single expression for various boundary conditions, including the classical cases (i.e., simply supported, free, and clamped). In addition, the solution presented was verified using published results for the classical boundary conditions and an FE model that considered edges elastically restrained as to translation and rotation. An example of a slab with simply supported and clamped edges also demonstrated a step-by-step procedure to implement the derived stability equation.

It was shown that the effects of the semirigid connections on the critical load were coupled to each other: The rotational spring greatly influenced the critical load as long as the translational spring had relevant magnitude. Furthermore, in analysis of a typical concrete pavement, it was found that the boundary conditions are of great relevance not only to the buckling load but also on the first buckling-mode shape. It was shown how as the joint deficiency diminished (i.e., reducing spring constants), the point of maximum deflection in the buckling-mode shape shifted from the slab's center to the edges. Finally, the relevance of the slab's aspect ratio on static buckling increased as boundary conditions became stiffer. However, the influence significantly decreased for large aspect ratios. From a practical point of view, it can be concluded that the likelihood of concrete pavement blowup can be reduced in the design phase by reducing the slab's aspect ratio and in the maintenance stage by keeping the joints in good condition.

6. SUMMARY AND CONCLUSIONS

Experimental measurements, the FE method, and closed-form solutions were combined to study the response to temperature changes of rigid pavement with partially restrained edges. Three models were developed. First, Westergaard's solution for curling stresses was extended to include edges with generalized boundary conditions. The closed-form solution obtained was verified with the FE method. Second, a FE model was developed to determine the curling responses of a multilayer airfield pavement with partially restrained edges. The model was validated with experimental measurements from the John F. Kennedy International Airport. Third, a closed-form solution for blowup analysis of a rectangular slab resting on an elastic foundation was found. This solution was also verified using the FE method. Based on the analysis performed, the following conclusions can be drawn:

- The ability of joints to transfer shear force and bending moment across a slab significantly affects maximum deflection and stresses caused by temperature gradients.
- Partial rotational restraint, which is not considered in conventional analysis and design of rigid pavements, is responsible for most of the difference when free edges are taken as reference.
- The influences of partial restraint as to displacement and rotation along slab edges on blowup behavior are coupled with each other; the relevance of rotational restriction increases as the magnitude of the translational spring increases.
- The ratio between the slab width and the radius of relative stiffness determines how much larger the curling stresses in a square slab are compared to those in an infinite slab. More specifically, joint condition is more relevant in short slabs. In addition, the slab's aspect ratio becomes relevant in the calculation of buckling load when there is good load-transfer efficiency in vertical displacement and rotation.

7. REFERENCES

ABAQUS. (2014). *ABAQUS 6.14* [Documentation]. Dassault Systèmes Simulia Corporation.

Alavi, S., LeCates, J. F., and Tavares, M. P. (2008). *Falling weight deflectometer usage—a synthesis of highway practice* (National Cooperative Highway Research Program Synthesis 381). Transportation Research Board. https://doi.org/10.17226/13675

Applied Research Associates, Inc. ERES Consultants Division. (2004). *Guide for mechanistic–empirical design of new and rehabilitated pavement structures* (Final report NCHRP 1-37A).

Areiza-Hurtado, M., Vega-Posada, C., & Aristizabal-Ochoa, J. D. (2005). Second-order stiffness matrix and loading vector of a beam-column with semirigid connections on an elastic foundation. *Journal of Engineering Mechanics*, *131*(7), 752–762. https://doi.org/10.1061/(ASCE)0733-9399(2005)131:7(752)

Asbahan, R. E., & Vandenbossche, J. M. (2011). Effects of temperature and moisture gradients on slab deformation for jointed plain concrete pavements. *Journal of Transportation Engineering*, *137*(8), 563–570.

Beckemeyer, C., Khazanovich, L., & Yu, T. H. (2002). Determining amount of built-in curling in jointed plain concrete pavement: case study of Pennsylvania I-80. *Transportation Research Record: Journal of the Transportation Research Board*, *1809*(1), 85–92. https://doi.org/10.3141/1809-10

Ceylan, H., Gopalakrishnan, K., Kim, S., Taylor, P., Alhasan, A. A., & Yang, S. (2016). *Impact of curling and warping on concrete pavement.* Program for Sustainable Pavement Engineering and Research, Institute for Transportation, Iowa State University. https://lib.dr.iastate.edu/cgi/viewcontent.cgi?referer=&httpsredir=1&article=1118&context=intrans_techtransfer

Davids, W. G. (2000). Effect of dowel looseness on response of jointed concrete pavements. *Journal of Transportation Engineering*, *126*(1), 50–57. https://doi.org/10.1061/(ASCE)0733-947X(2000)126:1(50)

Davids, W. G., & Mahoney, J. P. (1999). Experimental verification of rigid pavement joint load transfer modeling with EverFE. *Transportation Research Record: Journal of the Transportation Research Board*, *1684*(1), 81-89. https://doi.org/10.3141%2F1684-10

Federal Highway Administration (1990). *Concrete pavement joints* (Technical advisory T 5040.30). https://www.fhwa.dot.gov/pavement/t504030.cfm

Garg, N., Flynn, R. M., Pecht, F., & Brill, D. R. (2013). FAA's instrumentation project at John F. Kennedy International Airport to study load and environment induced responses in concrete pavements [Article]. In *Ninth International Conference on the Bearing Capacity of Roads, Railways and Airfields* (Vol.1).

Guo, H., Sherwood, J. A., & Snyder, M. B. (1995). Component dowel-bar model for load-transfer systems in PCC pavements. *Journal of Transportation Engineering*, *121*(3), 289–298.

Haario, H., Saksman, E., & Tamminen, J. (2001). An adaptive metropolis algorithm. *Bernoulli*, *7*(2), 223–242. https://doi.org/10.2307/3318737

Hiller, J. E., & Roesler, J. R. (2010). Simplified nonlinear temperature curling analysis for jointed concrete pavements. *Journal of Transportation Engineering*, *136*(7): 654–663. https://doi.org/10.1061/(ASCE)TE.1943-5436.0000130

Huang, Y. H. (2004). *Pavement analysis and design* (2nd ed.). Pearson Prentice Hall.

Ioannides, A., Davis, C., & Weber, C. (1999). Westergaard curling solution reconsidered. *Transportation Research Record: Journal of the Transportation Research Board*, *1684*(1), 61–70. https://doi.org/10.3141/1684-08

Ioannides, A. M., and Khazanovich, L. (1998). Nonlinear temperature effects on multilayered concrete pavements. *Journal of Transportation Engineering*, *124*(2), 128–136. https://doi.org/10.1061/(ASCE)0733-947X(1998)124:2(128)

Joshi, A., Mehta, Y., Cleary, D., Henry, S., & Cunliffe, C. (2012). Load transfer efficiency of rigid airfield pavement: relationship to design thickness and temperature curling. *Transportation Research Record: Journal of the Transportation Research Board*, *2300*(1), 68–74. https://doi.org/10.3141%2F2300-08

Kennedy, M. C., & O'Hagan, A. (2001). Bayesian calibration of computer models. *Journal of the Royal Statistical Society: Series B (Statistical Methodology)*, *63*(3), 425–464. https://doi.org/10.1111/1467-9868.00294

Kerr, A. D. (1997). Assessment of concrete pavement blowups. *Journal of Transportation Engineering*, *123*(2), 123–131. https://doi.org/10.1061/(ASCE)0733-947X(1997)123:2(123)

Kerr, A. D. (1994). Blowup of a concrete pavement adjoining a rigid structure. *International Journal of Non-Linear Mechanics*, *29*(3), 387–396. https://doi.org/10.1016/0020-7462(94)90009-4

Kerr, A. D., & Dallis, W. A., Jr. (1985). Blowup of concrete pavements. *Journal of Transportation Engineering*, *111*(1), 33–53. https://doi.org/10.1061/(ASCE)0733-947X(1985)111:1(33)

Kerr, A. D., & Shade, P. J. (1984). Analysis of concrete pavement blowups. *Acta Mechanica*, *52*(3/4), 201–224. https://doi.org/10.1007/BF01179617

Khazanovich, L., & Gotlif, A. (2003). *Evaluation of joint and crack load transfer final report* (No. FHWA-RD-02-088). U.S. Department of Transportation Federal Highway Administration.

Kim, J., & Hjelmstad, K. (2003). Three-dimensional finite element analysis of doweled joints for airport pavements. *Transportation Research Record: Journal of the Transportation Research Board*, *1853*, 100–109. https://doi.org/10.3141%2F1853-12

Kim, S.-M. (2004). Buckling and vibration of a plate on elastic foundation subjected to in-plane compression and moving loads. *International Journal of Solids and Structures*, *41*(20), 5647–5661. https://doi.org/10.1016/j.ijsolstr.2004.05.006

Liang, R. Y., & Niu, Y.-Z. (1998). Temperature and curling stress in concrete pavements: Analytical solutions. *Journal of Transportation Engineering*, *124*(1), 91–100. https://doi.org/10.1061/(ASCE)0733-947X(1998)124:1(91)

Lytton, R. L., Pufahl, D. E., Michalak, C. H., Liang, H. S., & Dempsey, B. J. (1993). *An integrated model of the climatic effects on pavements* (FHWA-RD-90-033). U.S. Department of Transportation Federal Highway Administration.

Mohamed, A., & Hansen, W. (1997). Effect of nonlinear temperature gradient on curling stress in concrete pavements. *Transportation Research Record: Journal of the Transportation Research Board*, *1568*, 65–71. https://doi.org/10.3141%2F1568-08

Nishizawa, T., Fukuda, T., Matsuno, S., & Himeno, K. (1996). Curling stress equation for transverse joint edge of a concrete pavement slab based on finite-element method analysis. *Transportation Research Record: Journal of the Transportation Research Board, 1525*, 35–43. https://doi.org/10.1177/0361198196152500105

Richardson, J. M., & Armaghani, J. M. (1987). Stress caused by temperature gradient in portland cement concrete pavements. *Transportation Research Record: Journal of the Transportation Research Board*, *1121*, 7–13. http://onlinepubs.trb.org/Onlinepubs/trr/1987/1121/1121-002.pdf

Seide, P. (1958). Compressive buckling of a long simply supported plate on an elastic foundation. *Journal of the Aerospace Sciences, 25*(6), 382–384. https://doi.org/10.2514/8.7691

Sen, S., & Roesler, J. (2016). Contextual heat island assessment for pavement preservation. *International Journal of Pavement Engineering*, *19*(10), 865–873. https://doi.org/10.1080/10298436.2016.1213842

Shoukry, S. N., Fahmy, M., Prucz, J., & William, G. (2007). Validation of 3DFE analysis of rigid pavement dynamic response to moving traffic and nonlinear temperature gradient effects. *International Journal of Geomechanics*, *7*(1), 16–24. https://doi.org/10.1061/(ASCE)1532-3641(2007)7:1(16)

Siddique, Z. Q., Hossain, M., & Meggers, D. (2005). Temperature and curling measurements on concrete pavement. In *Proceedings of the 2005 Mid-Continent Transportation Research Symposium.* Center for Transportation Research and Education.

Tang, T., Zollinger, D. G., & Senadheera, S. (1993). Analysis of concave curling in concrete slabs. *Journal of Transportation Engineering*, *119*(4), 618–633. https://doi.org/10.1061/(ASCE)0733-947X(1993)119:4(618)

Timoshenko, S. P., & Woinowsky-Krieger, S. (1959). *Theory of plates and shells.* McGraw-Hill.

Wang, C. M., Wang, C. Y., & Reddy, J. N. (2004). *Exact solutions for buckling of structural members* (1st ed.). CRC Press. https://doi.org/10.1201/9780203483534

Wang, Q., & Chen, Y. (2011). Improvements to modeling of concrete slab curling by using NIKE3D finite element program. *Transportation Research Record: Journal of the Transportation Research Board*, *2226*, 71–81. https://doi.org/10.3141%2F2226-08

Wei, Y., Gao, X., Wang, F., & Zhong, Y. (2019). Nonlinear strain distribution in a field-instrumented concrete pavement slab in response to environmental effects. *Road Materials and Pavement Design*, *20*(2), 367–380. https://doi.org/10.1080/14680629.2017.1395353

Westergaard, H. (1927). Analysis of stresses in concrete pavements due to variations of temperature. *Highway Research Board Proceedings*, *6*, 201–215.

William, G. W., & Shoukry, S. N. (2001). 3D finite element analysis of temperature-induced stresses in dowel jointed concrete pavements. *International Journal of Geomechanics*, *1*(3), 291–307. https://doi.org/10.1061/(ASCE)1532-3641(2001)1:3(291)

Yoo, P. J., Al-Qadi, I. L., Elseifi, M. A., & Janajreh, I. (2006). Flexible pavement responses to different loading amplitudes considering layer interface condition and lateral shear forces. *The International Journal of Pavement Engineering*, *7*(1), 73–86. https://doi.org/10.1080/10298430500516074

Yu, H., Khazanovich, L., Darter, M., & Ardani, A. (1998). Analysis of concrete pavement responses to temperature and wheel loads measured from instrumented slabs. *Transportation Research Record*, *1639*(1), 94–101. https://doi.org/10.3141/1639-10

Yu, L. and Wang, C. (2008). Buckling of rectangular plates on an elastic foundation using the Levy method. *American Institute of Aeronautics and Astronautics Journal*, *46*(12), 3163–3167. https://doi.org/10.2514/1.37166

APPENDIX A—LINEAR SYSTEM OF EQUATIONS AND SOLUTION FOR SLAB-ON-GRADE SYSTEMS

Appendix A lists a linear system of equations and solution for slab-on-grade systems, which are discussed in section 3.1 of the main document.

Linear system of equations in matrix form is as follows:

$$\begin{bmatrix} A_{11} & A_{12} & A_{13} & A_{14} \\ A_{21} & A_{22} & A_{23} & A_{24} \\ A_{31} & A_{32} & A_{33} & A_{34} \\ A_{41} & A_{42} & A_{43} & A_{44} \end{bmatrix} \times \begin{bmatrix} C_1 \\ C_2 \\ C_3 \\ C_4 \end{bmatrix} = \begin{bmatrix} b_1 \\ b_2 \\ b_3 \\ b_4 \end{bmatrix} \quad \text{(A.1)}$$

The entries in the coefficient matrix are:

$$A_{11} = R_b \cosh\lambda \sin\lambda + \sqrt{2} \sinh\lambda \sin\lambda - R_b \cos\lambda \sinh\lambda \quad \text{(A.2)}$$
$$A_{12} = R_b \cos\lambda \cosh\lambda + R_b \sin\lambda \sinh\lambda + \sqrt{2} \cos\lambda \sinh\lambda \quad \text{(A.3)}$$
$$A_{13} = R_b \cos\lambda \cosh\lambda - \sqrt{2} \sin\lambda \cosh\lambda - R_b \sin\lambda \sinh\lambda \quad \text{(A.4)}$$
$$A_{14} = -R_b \cosh\lambda \sin\lambda - R_b \cos\lambda \sinh\lambda - \sqrt{2} \cos\lambda \cosh\lambda \quad \text{(A.5)}$$
$$A_{21} = R_a \cosh\lambda \sin\lambda + \sqrt{2} \sinh\lambda \sin\lambda - R_a \cos\lambda \sinh\lambda \quad \text{(A.6)}$$
$$A_{22} = -R_a \cos\lambda \cosh\lambda - \sqrt{2} \cos\lambda \sinh\lambda - R_a \sin\lambda \sinh\lambda \quad \text{(A.7)}$$
$$A_{23} = -R_a \cos\lambda \cosh\lambda + \sqrt{2} \sin\lambda \cosh\lambda + R_a \sin\lambda \sinh\lambda \quad \text{(A.8)}$$
$$A_{24} = -R_a \cosh\lambda \sin\lambda - R_a \cos\lambda \sinh\lambda - \sqrt{2} \cos\lambda \cosh\lambda \quad \text{(A.9)}$$
$$A_{31} = -\cosh\lambda \sin\lambda - \cos\lambda \sinh\lambda + \sqrt{2}\, T_b \cos\lambda \cosh\lambda \quad \text{(55)}$$
$$A_{32} = -\cos\lambda \cosh\lambda - \sqrt{2} T_b \sin\lambda \cosh\lambda + \sin\lambda \sinh\lambda \quad \text{(A.11)}$$
$$A_{33} = \cos\lambda \cosh\lambda - \sqrt{2} T_b \cos\lambda \sinh\lambda + \sin\lambda \sinh\lambda \quad \text{(A.12)}$$
$$A_{34} = -\cosh\lambda \sin\lambda + \sqrt{2} T_b \sinh\lambda \sin\lambda + \cos\lambda \sinh\lambda \quad \text{(A.13)}$$
$$A_{41} = \cosh\lambda \sin\lambda + \cos\lambda \sinh\lambda - \sqrt{2} T_a \cos\lambda \cosh\lambda \quad \text{(A.14)}$$
$$A_{42} = -\cos\lambda \cosh\lambda - \sqrt{2}\, T_a \sin\lambda \cosh\lambda + \sin\lambda \sinh\lambda \quad \text{(A.15)}$$
$$A_{43} = \cos\lambda \cosh\lambda - \sqrt{2} T_a \cos\lambda \sinh\lambda + \sin\lambda \sinh\lambda \quad \text{(A.16)}$$
$$A_{44} = \cosh\lambda \sin\lambda - \sqrt{2} T_a \sinh\lambda \sin\lambda - \cos\lambda \sinh\lambda \quad \text{(A.17)}$$

The entries in the b-matrix:

$$b_1 = \sqrt{2}\,(1 + \nu)\, \alpha\, \Delta T \frac{l^2}{h} \quad \text{(A.18)}$$
$$b_2 = \sqrt{2}\,(1 + \nu) \alpha\, \Delta T \frac{l^2}{h} \quad \text{(A.19)}$$
$$b_3 = 0 \quad \text{(A.20)}$$
$$b_4 = 0 \quad \text{(A.21)}$$

The terms in the solution for displacements:

$$
\begin{aligned}
c_1 \;=\; & [R_a\,(T_a + 2T_b) + R_b(2T_a + T_b) - 4\,T_aT_b + 2]\sin^3\lambda\sinh\lambda \\
& + \sqrt{2}[-R_a\,T_a\,T_b + R_a - R_b\,T_a\,T_b + R_b - 2\,(T_a + T_b)]\cos^3\lambda\sinh\lambda \\
& + (-R_a\,T_a - R_b\,T_b - 2)\cos^3\lambda\cosh\lambda \\
& + \sqrt{2}(R_a + R_b + T_a + T_b)\cos\lambda\sinh^3\lambda \\
& + \sqrt{2}\,[T_a\,(R_a\,T_b + R_b\,T_b - 1) - T_b]\cos\lambda\sinh\lambda \\
& + (R_a\,T_a + R_b\,T_b + 2)\cos\lambda\cosh^3\lambda\} \\
& - \sqrt{2}[R_a\,T_a\,T_b + R_a + R_b\,T_a\,T_b + R_b + 2\,(T_a + T_b)]\sin\lambda\cosh^3\lambda \\
& + \sqrt{2}(R_a + R_b - T_a - T_b)\sin^3\lambda\cosh\lambda \\
& + \sqrt{2}[T_a\,(R_aT_b + R_b\,T_b - 1) - T_b]\sin\lambda\cosh\lambda \\
& - 3[R_a\,(T_a + 2\,T_b) + R_b\,(2\,T_a + T_b) - 4\,T_a\,T_b + 2]\sin\lambda\cos^2\lambda\sinh\lambda \\
& + 3\,\sqrt{2}\,(-R_a - R_b + T_a + T_b)\,\sin\lambda\,\cos^2\lambda\,\cosh\lambda\, + 3\sqrt{2}\,[R_a\,(T_a\,T_b \\
& - 1) + R_b\,(T_a\,T_b - 1) + 2\,(T_a + T_b)]\,\sin^2\lambda\cos\lambda\sinh\lambda\, + 3\sqrt{2}\,(R_a \\
& + R_b + T_a + T_b)\cos\lambda\,\sinh\lambda\cosh^2\lambda\, + 3\sin^2\lambda\cos\lambda\cosh\lambda\,(R_aT_a \\
& + R_bT_b + 2) + 3\,(R_a\,T_a + R_b\,T_b + 2)\cos\lambda\sinh^2\lambda\cosh\lambda - 3\,[R_a\,(T_a \\
& + 2\,T_b) + R\_b\,(2\,T_a + T_b) + 4\,T_a\,T_b + 2]\sin\lambda\sinh\lambda\cosh^2\lambda \\
& -\, 3\,\sqrt{2}\,[R_a\,T_a\,T_b + R_a + R_b\,T_a\,T_b + R_b \\
& + 2\,(T_a + T_b)]\sin\lambda\sinh^2\lambda\cosh\lambda
\end{aligned}
\tag{A.22}
$$

$$
\begin{aligned}
c_2 \;=\; & \sqrt{2}\;(R_a - R_b)(T_aT_b - 1)\sin^3\lambda\sinh\lambda\; + \sqrt{2}(-R_a + R_b - T_a + T_b)\sin\lambda\;\sinh^3\lambda \\
& + \sqrt{2}\,[T_a\,(-R_a\,T_b + R_b\,T_b - 1) + T_b]\sin\lambda\;\sinh\lambda \\
& + \;[R_a\,(T_a + 2\,T_b) - R_b\,(2\,T_a + T_b)]\cos^3\lambda\;\sinh\lambda \\
& + \sqrt{2}\,(R_a - R_b - T_a + T_b)\cos^3\lambda\cosh\lambda \\
& + [R_b\,(2\,T_a + T_b) - R_a\,(T_a + 2\,T_b)]\cos\lambda\sinh^3\lambda \\
& + (2\,R_a\,T_a - 2\,R_b\,T_b)\cos\lambda\;\sinh\lambda \\
& - \sqrt{2}\,(R_a - R_b)(T_a\,T_b + 1)\cos\lambda\cosh^3\lambda \\
& + \sqrt{2}\;(R_a\,T_a\,T_b - R_b\,T_a\,T_b + T_a - T_b)\cos\lambda\cosh\lambda \\
& + (R_bT_b - R_aT_a)\sin\lambda\cosh^3\lambda\; + (R_aT_a - R_bT_b)\sin^3\lambda\;\cosh\lambda \\
& - 3\,\sqrt{2}(R_a - R_b)(T_a\,T_b - 1)\sin\lambda\cos^2\lambda\sinh\lambda \\
& + 3(R_b\,T_b - R_a\,T_a)\sin\lambda\cos^2\lambda\cosh\lambda \\
& + 3[\,R_b\,(2\,T_a + T_b) -\; R_a\,(T_a + 2T_b)]\sin^2\lambda\;\cos\lambda\sinh\lambda \\
& + 3[\,R_b\,(2\,T_a + T_b) -\; R_a\,(T_a + 2\,T_b)]\cos\lambda\sinh\lambda\cosh^2\lambda \\
& + 3\,\sqrt{2}(-R_a + R_b + T_a - T_b)\sin^2\lambda\;\cos\lambda\;\cosh\lambda \\
& - 3\,\sqrt{2}(R_a - R_b)(T_a\,T_b + 1)\cos\lambda\;\sinh^2\lambda\;\cosh\lambda \\
& + 3\,\sqrt{2}(-R_a + R_b - T_a + T_b)\sin\lambda\;\sinh\lambda\cosh^2\lambda \\
& + 3(R_b\,T_b -\; R_a\,T_a)\sin\lambda\sinh^2\lambda\cosh\lambda
\end{aligned}
\tag{A.23}
$$

$$
\begin{aligned}
c_3 \;=\; & \sqrt{2}\,(R_a - R_b - T_a + T_b)\sin^3\lambda\,\sinh\lambda \;+\sqrt{2}\,(R_a - R_b)(T_a\,T_b + 1)\sin\lambda\,\sinh^3\lambda \\
& + \sqrt{2}\,(R_a\,T_a\,T_b - R_b\,T_a\,T_b + T_a - T_b)\sin\lambda\sinh\lambda \;+ (R_b\,T_b - R_a\,T_a)\cos^3\lambda\sinh\lambda \\
& - \sqrt{2}\,(R_a - R_b)(T_a\,T_b - 1)\cos^3\lambda\cosh\lambda \;+ (R_b\,T_b - R_a\,T_a)\cos\lambda\,\sinh^3\lambda \\
& + \sqrt{2}(-R_a + R_b - T_a + T_b)\cos\lambda\,\cosh^3\lambda \\
& + \sqrt{2}(R_a T_a T_b - R_b T_a T_b + T_a - T_b)\,\cos\lambda\,\cosh\lambda \\
& + \,[R_a\,(T_a + 2\,T_b) - R_b\,(2\,T_a + T_b)]\sin\lambda\,\cosh^3\lambda \\
& + [R_a\,(T_a + 2\,T_b) - R_b\,(2\,T_a + T_b)]\sin^3\lambda\,\cosh\lambda \;+\; 2(R_a\,T_a \;-\; R_b T_b)\sin\lambda\,\cosh\lambda \\
& + 3\,\sqrt{2}(-R_a + R_b + T_a - T_b)\sin\lambda\cos^2\lambda\sinh\lambda \\
& + 3[R_b\,(2\,T_a + T_b) - R_a\,(T_a + 2\,T_b)]\sin\lambda\cos^2\lambda\cosh\lambda \\
& + 3(R_a T_a \;-\; R_b T_b)\sin^2\lambda\,\cos\lambda\,\sinh\lambda \;+ 3(R_b T_b - R_a T_a)\cos\lambda\sinh\lambda\cosh^2\lambda \\
& + 3\,\sqrt{2}(R_a - R_b)(T_a T_b - 1)\sin^2\lambda\,\cos\lambda\,\cosh\lambda \\
& + 3\,\sqrt{2}\,(-R_a + R_b - T_a + T_b)\cos\lambda\,\sinh^2\lambda\,\cosh\lambda \\
& + 3\sqrt{2}(R_a - R_b)\,(T_a\,T_b + 1)\sin\lambda\sinh\lambda\cosh^2\lambda \\
& + 3[R_a(T_a + 2\,T_b) - R_b\,(2\,T_a + T_b)]\sin\lambda\sinh^2\lambda\cosh\lambda
\end{aligned}
\tag{A.24}
$$

$$
\begin{aligned}
c_4 \;=\; & (R_a T_a + R_b T_b + 2)\sin^3\lambda\,\sinh\lambda \;+ (R_a\,T_a + R_b\,T_b + 2)\sin\lambda\,\sinh^3\lambda \\
& + \,\sqrt{2}(R_a + R_b - T_a - T_b)\cos^3\lambda\,\sinh\lambda \\
& + [R_a\,(T_a + 2\,T_b) + R_b\,(2\,T_a + T_b) - 4\,T_a\,T_b + 2]\cos^3\lambda\,\cosh\lambda \\
& + \sqrt{2}\,[R_a\,T_a\,T_b + R_a + R_b\,T_a\,T_b + R_b + 2\,(T_a + T_b)]\cos\lambda\,\sinh^3\lambda \\
& + \sqrt{2}\,[T_a\,(R_a\,T_b + R_b\,T_b - 1) - T_b]\cos\lambda\sinh\lambda \\
& + [R_a\,(T_a + 2\,T_b) + R_b\,(2\,T_a + T_b) + 4\,T_a\,T_b + 2]\cos\lambda\cosh^3\lambda \\
& + 2\,(R_a\,T_a + R_b\,T_b - 2)\cos\lambda\cosh\lambda \;+\sqrt{2}(R_a + R_b + T_a + T_b)\sin\lambda\cosh^3\lambda \\
& + \sqrt{2}\,[R_a\,(T_a\,T_b - 1) + R_b\,(T_a\,T_b - 1) + 2\,(T_a + T_b)]\sin^3\lambda\cosh\lambda \\
& + \sqrt{2}\,[T_b - T_a\,(R_a\,T_b + R_b\,T_b - 1)]\sin\lambda\,\cosh\lambda \\
& - 3\,(R_a\,T_a + R_b\,T_b + 2)\sin\lambda\,\cos^2\lambda\,\sinh\lambda \\
& - 3\,\sqrt{2}\,[R_a\,(T_a\,T_b - 1) + R_b\,(T_a\,T_b - 1) + 2\,(T_a + T_b)]\sin\lambda\,\cos^2\lambda\,\cosh\lambda \\
& + 3\,\sqrt{2}(-R_a - R_b + T_a + T_b)\sin^2\lambda\cos\lambda\,\sinh\lambda \\
& + 3\,\sqrt{2}\,[R_a\,T_a\,T_b + R_a + R_b\,T_a\,T_b + R_b + 2\,(T_a + T_b)]\cos\lambda\sinh\lambda\cosh^2\lambda \\
& - 3\,[R_a\,(T_a + 2\,T_b) + R_b\,(2\,T_a + T_b) - 4\,T_a\,T_b + 2]\sin^2\lambda\cos\lambda\cosh\lambda \\
& + 3\,[R_a\,(T_a + 2\,T_b) + R_b\,(2\,T_a + T_b) + 4\,T_a\,T_b + 2]\cos\lambda\sinh^2\lambda\cosh\lambda \\
& + 3\,(R_a\,T_a + R_b T_b + 2)\sin\lambda\sinh\lambda\cosh^2\lambda \\
& + 3\sqrt{2}\,(R_a + R_b + T_a + T_b)\,\sin\lambda\sinh^2\lambda\cosh\lambda
\end{aligned}
\tag{A.25}
$$

$$
\begin{aligned}
Det(A) = & -[R_a\,(R_b\,(T_a T_b - 2) + T_a + 2T_b) + R_b(2T_a + T_b) - 2T_a T_b + 1]\cos 4\lambda \\
& - [R_a(R_b(T_a T_b + 2) + T_a + 2T_b) + R_b(2T_a + T_b) + 2T_a T_b + 1]\cosh 4\lambda \\
& + \sqrt{2}\,[-R_a\,(R_b\,(T_a + T_b) - T_a\;T_b + 1) + R_b\,T_a\,T_b - R_b + T_a + T_b]\sin 4\lambda \\
& - [R_a\,(T_b\,(R_b + T_a) + R_b\,T_a + 1) + R_b\,T_a\,T_b + R_b + T_a + T_b)]\;\sinh 4\lambda \;+ 2\,(R_a\,T_a \\
& - 1)\,(R_b\,T_b - 1)
\end{aligned}
\tag{A.26}
$$

APPENDIX B—TERMS IN THE CHARACTERISTIC STABILITY EQUATION

Appendix B provides terms in the characteristic stability equation, which is shown in section 5.1 of the main document.

The following definitions are used in tables B-1 through B-7:

$$C = k - 2\alpha^2\,(1-\nu) \tag{B.1}$$
$$F = k - \alpha^2\,(2-\nu) \tag{B.2}$$
$$G = \beta_1^2\,(\alpha^2\nu - \beta_2^2) - \beta_1\beta_2 C + \alpha^2\nu\,(\beta_2^2 + F) \tag{B.3}$$
$$H = \beta_1^2(\alpha^2\nu\ - \beta_2^2) + \beta_1\beta_2 C + \alpha^2\nu(\beta_2^2 + F) \tag{B.4}$$
$$J = (F + \beta_1^2)(\alpha^2\nu\ + \beta_2^2) \tag{B.5}$$
$$K = (F - \beta_2^2)(\alpha^2\,\nu\ - \beta_1^2) \tag{B.6}$$
$$L = 2\,\alpha^2 F\nu\ + \beta_2^2\,(k - 2\alpha^2) + \beta_1^2\,(2\alpha^2 + 2\,\beta_2^2 - k) \tag{B.7}$$
$$P = 2\alpha^2 - k + s^2 + t^2 \tag{B.8}$$
$$Q = -2\alpha^2 + k + 4s^2 \tag{B.9}$$
$$R = \alpha^4\nu^2 - P(s^2 + t^2) + \alpha^2\nu Q \tag{B.10}$$
$$\bar{P} = -2\,\alpha^2 + k + s^2 + t^2 \tag{B.11}$$
$$\bar{Q} = 2\alpha^2 - k + 4t^2 \tag{B.12}$$
$$\bar{R} = \bar{P}(s^2 + t^2) + \alpha^2\nu\,\bar{Q}^2 - \alpha^4\nu^2 \tag{B.13}$$

$$\begin{aligned} COEF_{CR,(5,6)} = {} & -\beta_1^4(\alpha^2\,\nu\ + \beta_2^2) + \beta_1^2\,(-\beta_2^4 + \alpha^2 F\nu\ + 2\beta_2^2\,F) \\ & + \alpha^2\,\beta_2^2\,\nu\ [-\alpha^2\ - (\nu\ - 2) + \beta_2^2\ - k] \end{aligned} \tag{B.14}$$

$$\begin{aligned} COEF_{CR,(5,16)} = {} & \beta_1^6(\alpha^2\nu + \beta_2^2)^2 - \alpha^4\beta_2^2\nu^2(F - \beta_2^2)^2 \\ & + \beta_1^2\,\{2\,\alpha^2\,\beta_2^6\,\nu + \alpha^4\,F^2\,\nu^2 + 4\,\alpha^2\beta_2^2F^2\nu \\ & + \beta_2^4 F\,[k - \alpha^2\,(3\nu\ + 2)]\} + \beta_1^4\,\{-\beta_2^6 + 2\,\alpha^4 F\nu^2 + 4\beta_2^4 F \\ & + \beta_2^2 F[\alpha^2\,(3\nu\ + 2) - k]\} \end{aligned} \tag{B.15}$$

$$COEF_{CR,(7,6)} = 2\beta_1^4 + \beta_2^4 - 2\alpha^2 F\nu\ +\ (\beta_1^2 - \beta_2^2)(k - 2\alpha^2) \tag{B.16}$$
$$COEF_{CCR,(9,6)} = -\alpha^4\nu^2 + (s^2 + t^2)(2\alpha^2 - k - 7s^2 + t^2) - \alpha^2\nu Q \tag{B.17}$$

$$\begin{aligned} COEF_{CCR,(11,6)} = {} & 4\alpha^2\nu[-k\,(4s^2 + t^2) + 2\alpha^2(4s^2 + t^2) + 12s^2t^2] \\ & - 4\alpha^4\nu^2(4s^2 + t^2) \\ & + 4(s^2 + t^2)[k(4s^2 - t^2) + 4s^4 - s^2(8\alpha^2 + 3t^2) + t^4 \\ & + 2\alpha^2t^2] \end{aligned} \tag{B.18}$$

$$
\begin{aligned}
COEF_{CCR,(11,16)} &= k^2[4s^6 + s^4(9t^2 - 8\alpha^2\nu) + s^2(4\alpha^4\nu^2 + 6t^4 - 6\alpha^2\nu t^2) \\
&+ (t^3 + \alpha^2\nu t)^2] + 4s^{10} + s^8(17t^2 - 16\alpha^2) \\
&+ 4s^6\{-2\alpha^4[(\nu - 2)\nu - 2] + 7t^4 + \alpha^2(6\nu - 11)t^2\} \\
&+ 2s^4\{8\alpha^6(\nu - 2)\,\nu + 11t^6 + 6\alpha^2(4\nu - 3)t^4 \\
&- \alpha^4[\nu(\nu + 22) - 18]t^2\} \\
&+ 4s^2[\alpha^8(\nu - 2)^2\,\nu^2 + 2t^8 + \alpha^2(6\nu - 1)t^6 \\
&+ \alpha^4(\nu(13\nu - 14) + 6)t^4 - 3\alpha^6(\nu\ - 2)\nu(2\nu - 1)t^2] \\
&+ t^2(-\alpha^4(\nu - 2)\nu + t^4 + 2\alpha^2t^2)^2 \\
&+ 2k\{4s^8 + s^6[11t^2 - 4\alpha^2(\nu + 2)]\} \\
&+ 2k\{s^4[-4\alpha^4(\nu - 4)\nu + 9t^4 + \alpha^2(11\nu\ - 18)t^2] \\
&- [t^2 - \alpha^2(\nu - 2)](t^3 + \alpha^2\nu t)^2\} + 2k\{s\text{^}2\,[4\,\alpha^2(\nu - 2)\nu^2 \\
&+ t^6 + 2\,\alpha^2(7\nu\ - 6)\,t\text{^}4 + 3\,\alpha^4(4 - 5\,\nu)\,\nu t^2]\}
\end{aligned}
\tag{B.19}
$$

Table B-1. Terms in Characteristic Stability Equation When D>0 and $2\alpha^2$-k>$\Delta^{0.5}$ (Case 1: Real Roots)

$[RT]$	$[TRIG]_1$ $\cosh(2b\beta_1 - 2b\beta_2)$	$[TRIG]_2$ $\cosh(2b\beta_1 + 2b\beta_2)$	$[TRIG]_3$ $\sinh(2b\beta_1 - 2b\beta_2)$	$[TRIG]_4$ $\sinh(2b\beta_1 + 2b\beta_2)$
$R_aT_aR_bT_b$	$2(\beta_1 + \beta_2)^2$	$-2(\beta_1 - \beta_2)^2$	0	0
$R_aT_aT_b$	0	0	$2(\beta_1 - \beta_2)(\beta_1 + \beta_2)^2$	$-2(\beta_1 - \beta_2)^2(\beta_1 + \beta_2)$
$R_aT_aR_b$	0	0	$-2\beta_1(\beta_1 - \beta_2)\beta_2(\beta_1 + \beta_2)^2$	$-2\beta_1(\beta_1 - \beta_2)^2\beta_2(\beta_1 + \beta_2)$
$R_bT_bR_a$	0	0	$-2\beta_1(\beta_1 - \beta_2)\beta_2(\beta_1 + \beta_2)^2$	$-2\beta_1(\beta_1 - \beta_2)^2\beta_2(\beta_1 + \beta_2)$
$R_bT_bT_a$	0	0	$2(\beta_1 - \beta_2)(\beta_1 + \beta_2)^2$	$-2(\beta_1 - \beta_2)^2(\beta_1 + \beta_2)$
R_aT_a	$-2(\beta_1 + \beta_2)^2G$	$2(\beta_1 - \beta_2)^2H$	0	0
R_bT_b	$-2(\beta_1 + \beta_2)^2G$	$2(\beta_1 - \beta_2)^2H$	0	0
R_aR_b	$2\beta_1^2\beta_2^2(\beta_1^2 - \beta_2^2)^2$	$-2\beta_1^2\beta_2^2(\beta_1^2 - \beta_2^2)^2$	0	0
T_aT_b	$2(\beta_1^2 - \beta_2^2)^2$	$-2(\beta_1^2 - \beta_2^2)^2$	0	0
R_bT_a	$-2\beta_1\beta_2(\beta_1^2 - \beta_2^2)^2$	$-2\beta_1\beta_2(\beta_1^2 - \beta_2^2)^2$	0	0
R_aT_b	$-2\beta_1\beta_2(\beta_1^2 - \beta_2^2)^2$	$-2\beta_1\beta_2(\beta_1^2 - \beta_2^2)^2$	0	0
R_a	0	0	$2\beta_1(\beta_1 - \beta_2)\beta_2(\beta_1 + \beta_2)^2G$	$2\beta_1(\beta_1 - \beta_2)^2\beta_2(\beta_1 + \beta_2)H$
R_b	0	0	$2\beta_1(\beta_1 - \beta_2)\beta_2(\beta_1 + \beta_2)^2G$	$2\beta_1(\beta_1 - \beta_2)^2\beta_2(\beta_1 + \beta_2)H$
T_a	0	0	$-2(\beta_1 - \beta_2)(\beta_1 + \beta_2)^2G$	$2(\beta_1 - \beta_2)^2(\beta_1 + \beta_2)H$
T_b	0	0	$-2(\beta_1 - \beta_2)(\beta_1 + \beta_2)^2G$	$2(\beta_1 - \beta_2)^2(\beta_1 + \beta_2)H$
1	$2(\beta_1 + \beta_2)^2G^2$	$-2(\beta_1 - \beta_2)^2H^2$	0	0

Table B-2. Terms in Characteristic Stability Equation When $\Delta>0$ and $2\alpha^2-k<\Delta^{0.5}$ (Case 2: Complex Roots)—Part 1

$[RT]$	$[TRIG]_1$ $\sin^2(b\beta_2)\sinh(2b\beta_1)$	$[TRIG]_2$ $\cos^2(b\beta_2)\cosh(2b\beta_1)$	$[TRIG]_3$ $\sin^2(b\beta_2)\cosh(2b\beta_1)$	$[TRIG]_4$ $\cos^2(b\beta_2)\sinh(2b\beta_1)$
$R_aT_aR_bT_b$	0	$-4\beta_1\beta_2$	$4\beta_1\beta_2$	0
$R_aT_aT_b$	$2\beta_2(\beta_1^2+\beta_2^2)$	0	0	$-2\beta_2(\beta_1^2+\beta_2^2)$
$R_aT_aR_b$	$-2\beta_1^2\beta_2(\beta_1^2+\beta_2^2)$	0	0	$2\beta_1^2\beta_2(\beta_1^2+\beta_2^2)$
$R_bT_bR_a$	$-2\beta_1^2\beta_2(\beta_1^2+\beta_2^2)$	0	0	$2\beta_1^2\beta_2(\beta_1^2+\beta_2^2)$
$R_bT_bT_a$	$2\beta_2(\beta_1^2+\beta_2^2)$	0	0	$-2\beta_2(\beta_1^2+\beta_2^2)$
R_aT_a	0	$2\beta_1\beta_2L$	$-2\beta_1\beta_2L$	0
R_bT_b	0	$2\beta_1\beta_2L$	$-2\beta_1\beta_2L$	0
R_aR_b	0	0	0	0
T_aT_b	0	0	0	0
R_bT_a	0	$2\beta_1\beta_2(\beta_1^2+\beta_2^2)^2$	$-2\beta_1\beta_2(\beta_1^2+\beta_2^2)^2$	0
R_aT_b	0	$2\beta_1\beta_2(\beta_1^2+\beta_2^2)^2$	$-2\beta_1\beta_2(\beta_1^2+\beta_2^2)^2$	0
R_a	$2\beta_1^2\beta_2(\beta_1^2+\beta_2^2)J$	0	0	$-2\beta_1^2\beta_2(\beta_1^2+\beta_2^2)J$
R_b	$2\beta_1^2\beta_2(\beta_1^2+\beta_2^2)J$	0	0	$-2\beta_1^2\beta_2(\beta_1^2+\beta_2^2)J$
T_a	$-2\beta_2(\beta_1^2+\beta_2^2)K$	0	0	$2\beta_2(\beta_1^2+\beta_2^2)K$
T_b	$-2\beta_2(\beta_1^2+\beta_2^2)K$	0	0	$2\beta_2(\beta_1^2+\beta_2^2)K$
1	0	$-4\beta_1\beta_2JK$	$4\beta_1\beta_2JK$	0

Table B-3. Terms in Characteristic Stability Equation When $\Delta>0$ and $2\alpha^2-k<\Delta^{0.5}$ (Case 2: Complex Roots)—Part 2

$[RT]$	$[TRIG]_5$ $\sin(b\beta_2)\cos(b\beta_2)\sinh(2b\beta$	$[TRIG]_6$ $\sin(b\beta_2)\cos(b\beta_2)\cosh(2b\beta$	$[TRIG]_7$ $\sin^2(b\beta_2)$	$[TRIG]_8$ $\cos^2(b\beta_2)$
$R_aT_aR_bT_b$	$-4(\beta_2^2-\beta_1^2)$	0	$4\beta_1\beta_2$	$4\beta_1\beta_2$
$R_aT_aT_b$	0	$4\beta_1(\beta_1^2+\beta_2^2)$	0	0
$R_aT_aR_b$	0	$4\beta_1\beta_2^2(\beta_1^2+\beta_2^2)$	0	0
$R_bT_bR_a$	0	$4\beta_1\beta_2^2(\beta_1^2+\beta_2^2)$	0	0
$R_bT_bT_a$	0	$4\beta_1(\beta_1^2+\beta_2^2)$	0	0
R_aT_a	$4COEF_{CR,(5,6)}$	0	$\beta_1\beta_2COEF_{CR,(7,6)}$	$\beta_1\beta_2COEF_{CR,(7,6)}$
R_bT_b	$4COEF_{CR,(5,6)}$	0	$\beta_1\beta_2COEF_{CR,(7,6)}$	$\beta_1\beta_2COEF_{CR,(7,6)}$
R_aR_b	$-4\beta_1^2\beta_2^2(\beta_1^2+\beta_2^2)^2$	0	0	0
T_aT_b	$4(\beta_1^2+\beta_2^2)^2$	0	0	0
R_bT_a	0	0	0	0
R_aT_b	0	0	0	0
R_a	0	$-4\beta_1\beta_2^2(\beta_1^2+\beta_2^2)K$	0	0
R_b	0	$-4\beta_1\beta_2^2(\beta_1^2+\beta_2^2)K$	0	0
T_a	0	$-4\beta_1(\beta_1^2+\beta_2^2)J$	0	0
T_b	0	$-4\beta_1(\beta_1^2+\beta_2^2)J$	0	0
1	$4COEF_{CR,(5,16)}$	0	$4\beta_1\beta_2JK$	$4\beta_1\beta_2JK$

Table B-4. Terms in Characteristic Stability Equation When Δ>0 (Case 3: Complex Conjugate Roots)—Part 1

$[RT]$	$[TRIG]_1$ $\cosh(4bs)\cos^4(bt)$	$[TRIG]_2$ $\sinh(4bs)\cos^4(bt)$	$[TRIG]_3$ $\cosh(4bs)\sin^4(bt)$	$[TRIG]_4$ $\sinh(4bs)\sin^4(bt)$	$[TRIG]_5$ $\sin^3(bt)\cos(bt)$
$R_aT_aR_bT_b$	$-2t^2$	0	$-2t^2$	0	0
$R_aT_aT_b$	0	$-4st^2$	0	$-4st^2$	$-16s^2t$
$R_aT_aR_b$	0	$-4st^2(s^2+t^2)$	0	$-4st^2(s^2+t^2)$	$16s^2t(s^2+t^2)$
$R_bT_bR_a$	0	$-4st^2(s^2+t^2)$	0	$-4st^2(s^2+t^2)$	$16s^2t(s^2+t^2)$
$R_bT_bT_a$	0	$-4st^2$	0	$-4st^2$	$-16s^2t$
R_aT_a	$2t^2R$	0	$2t^2R$	0	0
R_bT_b	$2t^2R$	0	$2t^2R$	0	0
R_aR_b	$-8s^2t^2(s^2+t^2)^2$	0	$-8s^2t^2(s^2+t^2)^2$	0	0
T_aT_b	$-8s^2t^2$	0	$-8s^2t^2$	0	0
R_bT_a	$-8s^2t^2(s^2+t^2)$	0	$-8s^2t^2(s^2+t^2)$	0	0
R_aT_b	$-8s^2t^2(s^2+t^2)$	0	$-8s^2t^2(s^2+t^2)$	0	0
R_a	0	$4st^2R(s^2+t^2)$	0	$4st^2R(s^2+t^2)$	$16s^2t\,\bar{R}\,(s^2+t^2)$
R_b	0	$4st^2R(s^2+t^2)$	0	$4st^2R(s^2+t^2)$	$16s^2t\bar{R}\,(s^2+t^2)$
T_a	0	$4st^2R$	0	$4st^2R$	$-16s^2t\bar{R}$
T_b	0	$4st^2R$	0	$4st^2R$	$-16s^2t\bar{R}$
1	$-2t^2R^2$	0	$-2t^2R^2$	0	0

Table B-5. Terms in Characteristic Stability Equation When Δ>0 (Case 3: Complex Conjugate Roots)—Part 2

$[RT]$	$[TRIG]_6$ $\sin(bt)\cos^3(bt)$	$[TRIG]_7$ $\cosh(4bs)\sin^2(bt)\cos^2(bt)$	$[TRIG]_8$ $\sinh(4bs)\sin^2(bt)\cos^2(bt)$	$[TRIG]_9$ $\sin^4(bt)$	$[TRIG]_{10}$ $\cos^4(bt)$
$R_aT_aR_bT_b$	0	$-4t^2$	0	$2t^2$	$2t\text{^}2$
$R_aT_aT_b$	$16s^2t$	0	$8st^2$	0	0
$R_aT_aR_b$	$-16s^2t(s^2+t^2)$	0	$-8st^2(s^2+t^2)$	0	0
$R_bT_bR_a$	$-16s^2t(s^2+t^2)$	0	$-8st^2(s^2+t^2)$	0	0
$R_bT_bT_a$	$16s^2t$	0	$-8st^2$	0	0
R_aT_a	0	$4t^2R$	0	$2t^2COEF_{CCR,(9,6)}$	$2t^2COEF_{CCR,(9,6)}$
R_bT_b	0	$4t^2R$	0	$2t^2COEF_{CCR,(9,6)}$	$2t^2COEF_{CCR,(9,6)}$
R_aR_b	0	$-16s^2t^2(s^2+t^2)^2$	0	$8s^2t^2(s^2+t^2)^2$	$8s^2t^2(s^2+t^2)^2$
T_aT_b	0	$-16s\text{^}2t\text{^}2$	0	$8s^2t^2$	$8s^2t^2$
R_bT_a	0	$-16s^2t^2(s^2+t^2)$	0	$-8s^2t^2(s^2+t^2)$	$-8s^2t^2(s^2+t^2)$
R_aT_b	0	$-16s^2t^2(s^2+t^2)$	0	$-8s^2t^2(s^2+t^2)$	$-8s^2t^2(s^2+t^2)$
R_a	$-16s^2t\,\bar{R}(s^2+t^2)$	0	$8st^2R(s^2+t^2)$	0	0
R_b	$-16s^2t\bar{R}(s^2+t^2)$	0	$8st^2R(s^2+t^2)$	0	0
T_a	$16s^2t\bar{R}$	0	$8st^2R$	0	0
T_b	$16s^2t\bar{R}$	0	$8st^2R$	0	0
1	0	$-4t^2R^2$	0	$2t^2R^2$	$2t^2R^2$

Table B-6. Terms in Characteristic Stability Equation When Δ<0
(Case 3: Complex Conjugate Roots)—Part 3

$[RT]$	$[TRIG]_{11}$ $\sin^2(bt)\cos^2(bt)$
$R_aT_aR_bT_b$	$4(4s^2+t^2)$
$R_aT_aT_b$	0
$R_aT_aR_b$	0
$R_bT_bR_a$	0
$R_bT_bT_a$	0
R_aT_a	$COEF_{CCR,(11,6)}$
R_bT_b	$COEF_{CCR,(11,6)}$
R_aR_b	$-48s^2t^2(s^2+t^2)^2$
T_aT_b	$-48s^2t^2$
R_bT_a	$48s^2t^2(s^2+t^2)$
R_aT_b	$48s^2t^2(s^2+t^2)$
R_a	0
R_b	0
T_a	0
T_b	0
1	$4COEF_{CCR,(11,16)}$

Table B-7. Terms in Characteristic Stability Equation not Multiplying Trigonometric Functions When Δ>0 and $2\alpha^2$-k>$\Delta^{0.5}$ (Case 1: Real Roots)

$[RT]$	$[TRIG]$
$R_aT_aR_bT_b$	$-8\beta_1\beta_2$
$R_aT_aT_b$	0
$R_aT_aR_b$	0
$R_bT_bR_a$	0
$R_bT_bT_a$	0
R_aT_a	$-4\beta_1\beta_2[\beta_1^4+\beta_2^4-2\alpha^2F\nu+\beta_1^2(k-2\alpha^2)+\beta_2^2(k-2\alpha^2)]$
R_bT_b	$-4\beta_1\beta_2[\beta_1^4+\beta_2^4-2\alpha^2F\nu+\beta_1^2(k-2\alpha^2)+\beta_2^2(k-2\alpha^2)]$
R_aR_b	0
T_aT_b	0
R_bT_a	0
R_aT_b	0
R_a	0
R_b	0
T_a	0
T_b	0
1	$-8\beta_1\beta_2(\beta_1^2+F)(\beta_2^2+F)(\alpha^2\nu-\beta_1^2)(\alpha^2\nu-\beta_2^2)$